Relativistic Effects and Polarization
in Three High-Energy Pulsar Models

J. Dyks[1], Alice K. Harding

Laboratory for High Energy Astrophysics, NASA/GSFC, Greenbelt, MD 20771, USA

`jinx@milkyway.gsfc.nasa.gov`, `harding@twinkie.gsfc.nasa.gov`

and

B. Rudak

Nicolaus Copernicus Astronomical Center, 87-100 Toruń, Poland

`bronek@ncac.torun.pl`

ABSTRACT

We present the influence of the special relativistic effects of aberration and light travel time delay on pulsar high-energy lightcurves and polarization characteristics predicted by three models: the two-pole caustic model, the outer gap model, and the polar cap model. Position angle curves and degree of polarization are calculated for the models and compared with the optical data on the Crab pulsar. The relative positions of peaks in gamma-ray and radio lightcurves are discussed in detail for the models. We find that the two-pole caustic model can reproduce qualitatively the optical polarization characteristics of the Crab pulsar – fast swings of the position angle and minima in polarization degree associated with both peaks. The anticorrelation between the observed flux and the polarization degree (observed in the optical band also for B0656+14) naturally results from the caustic nature of the peaks which are produced in the model due to the superposition of radiation from many different altitudes, ie. polarized at different angles. The two-pole caustic model also provides an acceptable interpretation of the main features in the Crab's radio profile. Neither the outer gap model nor the polar cap model are able to reproduce the optical polarization data on the Crab. Although the outer gap model is very successful in reproducing the relative positions of gamma-ray and radio peaks in pulse profiles, it can reproduce the high-energy lightcurves only when photon emission from regions very close to the light cylinder is included.

---

[1]On leave from Nicolaus Copernicus Astronomical Center, Toruń, Poland

Subject headings: pulsars: general — polarization — gamma rays: theory — radiation mechanisms: nonthermal

1.   Introduction

This paper focuses on two aspects of theoretical modelling of high-energy emission from pulsars: 1) the influence of special relativity effects on pulsar high-energy lightcurves, and 2) on linear polarization properties of the high-energy radiation.

The special relativity (SR) effects which affect the lightcurves include the aberration of photon emission directions and time of flight delays caused by the finite speed of light c. Their importance for lightcurve shapes was recognized by many pulsar astrophysicists long ago (eg. Harding et al. 1978; Massaro et al. 1979) but it was Morini (1983) who first proved that the SR effects themselves are able to produce prominent peaks in pulsar lightcurves. Morini obtained the peaks of caustic[1] origin in his version of the polar cap model because he included emission of photons by electrons propagating at high-altitudes, where the SR effects are important. The high altitude emission has been often ignored by polar cap theorists who have naturally focused on near-surface regions, where the strongest acceleration takes place and photons of highest energy are produced (Sturrock 1971; Ruderman & Sutherland 1975; Daugherty & Harding 1982; Sturner et al. 1995; Rudak & Dyks 1999). As does every contemporary model of pulsars, the polar cap model faces some difficulties with reproducing pulsar data. Perhaps the most serious of these problems is the difficulty in reproducing the wide separation between the two peaks commonly observed in the MeV-GeV lightcurves of the brightest gamma-ray pulsars (Kanbach 1999; Thompson 2001) without invoking very small inclination angle. We discuss the subject in more detail in Section 3.3.

In the recent version of the outer gap (OG) model (Romani & Yadigaroglu 1995; Cheng, Ruderman, Zhang (2000), hereafter CRZ2000) peaks in pulsar lightcurves are purely due to the caustic effects - a fact first emphasized by Romani & Yadigaroglu (1995) (hereafter RY95). However, an important additional factor which determines lightcurve shape in the OG model is the geometry of the acceleration region (outer gap). Although the performance of the OG model in reproducing pulsar lightcurves is relatively good, it fully relies on including photon emission from the very vicinity of the light cylinder - where the assumed vacuum magnetic field geometry is very questionable. Moreover, the "traditional" shape of the outer gap (extending from the null charge surface up to the light cylinder) has recently been

---

[1] The SR effects result directly in caustic effects (piling up photons at the same phase of a pulse). Therefore, hereafter we will use the terms "special relativity effects" and "caustic effects" as synonyms.

questioned (Hirotani & Shibata 2002), and this shape was crucial for getting the good-looking lightcurves.

In view of the problems faced by the afore-mentioned models, Dyks & Rudak (2003) introduced an alternative type of caustic model which assumes roughly uniform emission of photons along the entire length of all last open magnetic field lines, ie. photon emission in the model extends all the way from the pulsar surface up to the vicinity of the light cylinder. The emission is not restricted to the polar gap or to the outer gap region. There are good prospects that the slot gap model (Arons & Scharlemann 1979; Arons 1983) especially with the recent revisions by Muslimov & Harding (2003a) will provide a viable physical justification for the assumptions of the extended caustic model. Acceleration of electrons in regions outside the traditional outer gap (ie. below the null charge surface) has also been recently proposed by Wright (2003) in his empirical model of radio emission from pulsars. Given that the two-pole caustic model is extremely simple and robust in explaining pulsar lightcurves with widely separated double peaks we consider it as a serious alternative to both the outer gap and the polar cap model and we include it in our study.

So far, polarization of pulsar radiation has been most thoroughly studied within the polar cap model of coherent radio emission. A geometrical framework of the model was founded already by Radhakrishnan & Cooke (1969). Much later Blaskiewicz et al. (1991) furnished the model with lowest order special relativity effects. However, the noncoherent high-energy emission has a different spatial origin and requires a separate study. Polarization properties of the high-energy radiation have been concisely discussed for both the polar cap (Daugherty, Harding 1996) and the outer gap model (Romani Yadigaroglu 1995; Chen et al. 1996). We undertake the calculations and discussion again, because of the complexity of the subject, as well as because of access to new, excellent quality, optical polarization data on the Crab pulsar (Kanbach et al. 2003). Also, upcoming progress in high-energy polarimetry (Integral, Mega, Advanced Pair Telescope) makes the subject of polarization very important.

The paper is organized as follows: Section 2 describes the way in which we calculate lightcurves and polarization properties in the models described above. Section 3 presents our results. In Section 3.1 we discuss the two-pole caustic model, in Section 3.2 – the outer gap model, and in Section 3.3 – the polar cap model. Section 3.4 includes a discussion of relative positions of gamma-ray and radio peaks in pulsar lightcurves. Interpretation of radio pulse profile of the Crab pulsar within the two-pole caustic model is given there. Section 4 contains conclusions.

2. Calculation method

We assume that the magnetic field of a pulsar has the geometry of a vacuum dipole distorted by rotational effects, ie. we use the "retarded vacuum dipole" approximation, commonly encountered in previous research (eg. Romani & Yadigaroglu 1995; Arendt & Eilek 1998; Cheng et al. 2000). However, to enable estimate of the importance of near light-cylinder magnetic field distortions, we also present a limited number of results for the static shape dipole.

We perform Runge-Kutta integrations along magnetic field lines to determine a shape of the polar cap rim. With the polar cap rim determined, we calculate "open volume coordinates" (defined below) at the star surface to position footprints of those magnetic field lines along which photon emission is then followed. These steps are described in more detail in the following subsections. The photon emission is then modelled as follows: the field lines in a frame corotating with the star are divided into small segments, the length of which had been constrained by the pre-determined phase resolution of our calculation (typically 360 bins per rotation period). For each segment the position of emission point $\vec{r}_{\mathrm{em}}'$ and the direction of emission $\vec{\eta}_{\mathrm{em}}'$ in the (primed) corotating frame (CF) are determined. The emission direction is assumed to be along the electron velocity in the CF, ie. tangent to the magnetic field line. Then the Lorentz transformation of $\vec{\eta}_{\mathrm{em}}'$ (aberration) to the (unprimed) value in an inertial observer frame (IOF) is performed. The direction of photon propagation $\vec{\eta}_{\mathrm{em}}$ in the IOF along with $\vec{r}_{\mathrm{em}}$ determine the phase ϕ at which photons are observed. Time delays due to the finite speed of light are taken into account at this stage. The electric field vector of the emitted "wave" $\vec{E}_{\mathrm{w}}$ in IOF is determined in each step as follows: a new emission direction $\vec{\eta}_1'$ at a nearby emission point at the same magnetic field line is found, $\vec{\eta}_1'$ is rotated to account for the spin of the neutron star, and finally transformed to the IOF, where the difference between $\vec{\eta}_{\mathrm{em}}$ and $\vec{\eta}_1$ is used to calculate the acceleration of the electron at the emission point $\vec{a}$. We followed Blaskiewicz et al. (1991, hereafter BCW91) and Hibschman & Arons (2001, hereafter HA2001) by assuming that $\vec{E}_{\mathrm{w}}$ is parallel to $\vec{a}$. This approach differs from the method of Radhakrishnan & Cooke (1969) and RY95 who assumed that the vector $\vec{E}_{\mathrm{w}}$ has the direction of the curvature radius of a magnetic field line at the emission point which did not include the acceleration due to rotation. To emulate uniform intensity, the Stokes parameter I is simply assumed to be equal to the length of a field line segment. To calculate the parameters Q and U we use the position angle (PA) ψ between $\vec{E}_{\mathrm{w}}$ and the projection of the pulsar spin axis on the plane of the sky. Propagation effects are ignored and the emitted radiation is assumed to be linearly polarized at 80%. The values of I, Q, and U are then accumulated in (ie. added to those already present in) appropriate bins of 2D tables, the two dimensions of which correspond to the phase ϕ and to the observer's position $\zeta_{\mathrm{obs}} = (\vec{\eta}_{\mathrm{em}})_z$. After collecting photons from all field line segments appropriate for

a given model (eg. for the outer gap model, only outward emission from regions above the null charge surface is included), the final values of Stokes parameters (from the 2D tables) are transformed back into values of position angle $\psi = 0.5 \arctan(U/Q)$ and polarization percentage $P = (Q^2 + U^2)^{1/2}/I$.

Although the above description may give the impression that we followed exactly the methods from previous works (eg. RY95; CRZ2000), our calculation differs from them in a few important details which are discussed below.

2.1.   The shape of a polar cap

In previous studies (RY 95; Arendt, Eilek 1998; CRZ2000) the polar cap rim was determined via bisection in magnetic colatitude θ_m performed at fixed magnetic azimuths ϕ_m, with the latter spaced uniformly around the magnetic pole. This method resulted in a discontinuous rim shape – with a "jump" or a "glitch" at $\phi_\mathrm{m} \sim 115°$ for moderate dipole inclinations $\alpha = 40° - 50°$.

In our calculations, we applied bisection in the magnetic azimuth ϕ_m (at fixed θ_m) for the glitch part of the polar cap rim, and the traditional bisection in θ_m (at fixed ϕ_m) for the rest of the rim. This produced the interesting result presented with a thick solid line in Fig. 1 (for $\alpha = 45°$): the "glitch" actually appears to be a "notch" in the polar cap rim. The rim winds "backwards" at the notch, where, for a fixed magnetic azimuth ϕ_m, there are *three* solutions for the rim's magnetic colatitude θ_m.

The tip of the notch (marked with C1 in Fig. 1) is one of two "critical" points on the polar cap rim. The second critical point is marked by C2 in Fig. 1. The critical points divide the polar cap rim into 2 parts, denoted by R1 and R2 in Fig. 1. As first described by Yadigaroglu (1997), magnetic field lines emerging from the R1 part of the rim are tangent to the light cylinder at points forming a spiral line. Lines emerging from the R2 part of the rim are tangent to the light cylinder at points forming a different spiral. In this sense the rim of the polar cap consists of two different curves (R1, and R2) which meet at the critical points. As will become clear in Section 3, a high-altitude spread of magnetic field lines with footprints distributed uniformly along the polar cap rim, changes discontinuously at the critical points C1 and C2. This produces notable effects in lightcurves.

Although the electric field near polar gap should destroy (or at least smooth out) the notch, for definiteness we include it in our calculations. We find that the high-altitude spatial spread of magnetic field lines which emerge from the notch part of the polar cap rim (on the R1 side of the C1 point) is much larger than the high-altitude spread of lines emerging from

any other part of the polar cap rim, assuming uniform distribution of footprints along the rim. Therefore, neglecting the notch part of the polar cap rim results in a very large part of magnetosphere void of magnetic field lines. For $\alpha = 45°$, this "missed region" extends over more than a half of one quadrant of the magnetosphere (cf. fig. 2 in Arendt & Eilek 1998) .

2.2. Open volume coordinates

Rotational effects destroy the symmetry of the dipolar magnetic field around the dipole axis. Therefore the magnetic pole no longer provides a useful reference point at the stellar surface – the primary reference object becomes the rim of polar cap. This forced Yadigaroglu (1997) and CRZ2000 to introduce "open volume coordinates". One of the coordinates was the magnetic azimuth ϕ_m of a point at the star surface and the second one (denoted by a by CRZ2000) was equal to the ratio θ_m/θ_m^{rim}, where θ_m is the magnetic colatitude of that point, and θ_m^{rim} is the magnetic colatitude of the polar cap rim measured at ϕ_m. Yadigaroglu (1997) used a similar coordinate: $w = 1 - a$.

Although connected to the polar cap rim, these coordinates still refer to the magnetic pole and, therefore, have serious disadvantages: 1) they cannot be defined for moderate inclination angles $\alpha = 40° - 50°$ because of the ambiguity of rim colatitude at the notch; 2) even for cases without the notch (eg. for $\alpha > 60°$ often considered in the outer gap model), different points having the same value of a in general do not lie at the same distance from the polar cap rim.

Therefore, we introduce new open volume coordinates (r_{ovc}, l_{ovc}) to identify points at the star surface. The first coordinate is defined as $r_{ovc} = 1 \pm d_{ovc}$, where d_{ovc} is the minimum distance of a point from the polar cap rim normalized by the standard polar cap radius $r_{pc} = (\Omega R_{ns}^3 c^{-1})^{1/2}$; ($\Omega = 2\pi/P_{rot}$ is the angular velocity of pulsar rotation, P_{rot} is the rotation period, and R_{ns} is the radius of the neutron star). The plus sign refers to points lying outside the polar cap, the minus sign is for points within the cap. Thus, all points with, eg. $r_{ovc} = 0.9$ form a deformed ring (similar in shape to the polar cap rim) lying inside the polar cap at fixed distance $0.1 r_{pc}$ from the rim. For points at the rim $r_{ovc} = 1$. Rings of fixed r_{ovc} are shown in Fig. 2. For small ($\alpha \lesssim 30°$) and large ($\alpha \gtrsim 65°$) dipole inclinations, a, w, and r_{ovc} are approximately related by: $r_{ovc} \simeq a$, and $r_{ovc} \simeq 1 - w$.

The second coordinate l_{ovc} of a point located at a given r_{ovc} is the arclength measured along the deformed ring of fixed r_{ovc} at which the considered point lies. The arclength is measured in the direction of increasing ϕ_m (counterclockwise in Fig. 2), with $l_{ovc} = 0$ corresponding to $\phi_m = 0$.

Although being difficult to establish, the new open volume coordinates enable us to easily emulate useful electron distributions at the star surface; eg. to model photon emission due to a uniform distribution of electrons between some $r_{\rm ovc}^{\rm min}$ and $r_{\rm ovc}^{\rm max}$ we calculate the equidistant deformed rings within the considered range of $r_{\rm ovc}$, then we position magnetic field line footprints uniformly along each ring (ie. nonuniformly in $\phi_{\rm m}$). Since we follow photon emission for the same number of magnetic field lines for each ring, the emissivity for different rings is weighted by $l_{\rm ring}/l_{\rm rim}$, where $l_{\rm ring}$ is the "circumference" of a given ring, and $l_{\rm rim}$ is the "circumference" of the polar cap rim.

Since most contemporary pulsar models consider the last open magnetic field lines as a primary region of photon emission (or lines close to the last open) below we also consider a "rim dominated" electron density distribution at the star surface: we additionally weight the emissivity from different rings by a value of the Gaussian function:

$$\frac{dN_{\rm ph}}{ds} \propto \exp\left(-\frac{(r_{\rm ovc} - r_{\rm ovc}^0)^2}{2\sigma^2}\right) \tag{1}$$

with σ usually set equal to 0.025. The function is centered at the polar cap rim ($r_{\rm ovc}^0 = 1$, two-pole caustic model) or at $r_{\rm ovc}^0 = 0.9$ (outer gap model). Fig. 3 presents a sample distribution of magnetic field line footprints at the star surface for the lines along which photon emission is then followed.

2.3.   Assumed emissivity

For the two-pole caustic and for the outer gap model, we assume a uniform emissivity along the magnetic field lines as a useful preliminary approximation of actual photon emission. This approximation is reasonable since the electron energy may be stabilized within a very broad range of altitudes by the radiation reaction limited acceleration (eg. see fig. 10 in Hirotani et al. 2003). Without a reliable prescription for an altitude at which the emission ceases, the "cut-off" altitude becomes an important, additional parameter of our calculations.

Since the geometry of the dipolar magnetic field is not known close to the light cylinder, when modelling emission for the two-pole caustic model we assume that the emissivity drops sharply to zero at a distance $\rho_{\rm max}$ from the rotational axis, with $\rho_{\rm max}$ between 0.75 and $0.95 R_{\rm lc}$, where $R_{\rm lc} = c/\Omega$ is the radius of the light cylinder. This distinguishes our calculation from those of RY95, Yadigaroglu (1997), and CRZ2000, who assumed that the strong photon emission can be reliably traced up to $\rho_{\rm max} = R_{\rm lc}$. Given that the geometry of magnetic field lines close to the light cylinder should be strongly influenced by magnetospheric currents and particle inertia we do not consider the near-$R_{\rm lc}$ region of the vacuum retarded dipole

a good approximation of the real magnetic field. To support the vacuum retarded dipole it is often argued that it approximates the actual magnetosphere at least in the limit of low particle density, which is expected within vacuum gaps. However, since the open field lines are assumed to be a primary source for the bulk of gamma-ray emission they must be non-negligibly loaded with charged particles which makes the vacuum dipole approximation not applicable to them. Moreover, currents generated by charges which fill in regions outside the "vacuum" gaps (regions adjacent to the gaps in particular) should modify the magnetic field not only outside the gaps, but also inside them.

In the outer gap model the bulk of gamma rays comes from "open" field lines lying *close* to the last open lines – with $r_{ovc} \simeq 0.9$ (RY95, CRZ2000). However, the "close to last open" field lines in fact *close* just behind the light cylinder, where they should open to connect smoothly with a wind region. This change in the field line geometry would propagate inwards, and would influence the shape of field lines within, and close to the light cylinder.

Therefore, we argue that reliable outer gap calculations should be limited to $\rho_{max} \sim 0.8 R_{lc}$. However, outer gap pulse profiles calculated for $\rho_{max} = 0.8 R_{lc}$ do not exhibit the leading peak, which in the outer gap model forms very close to the light cylinder. Therefore, to allow for the leading peak to be formed, and to enable comparison with previous results below we present outer gap results for $\rho_{max} \approx R_{lc}$.

Apart from the emission boundary due to the proximity of the light cylinder, it is useful to constrain the photon emission to some limited distance from the star. This would take into account a probable decline of emissivity with increasing altitude. For example, Romani & Yadigaroglu (1995) assume a Gaussian decline in emissivity (with $\sigma = 0.5 R_{lc}$) at distances s measured along magnetic field lines larger than R_{lc}. In this paper we assume a constant radial distance from the star r_{max} as an additional upper boundary of the emission region. For $r > r_{max}$ we assume zero emissivity.

2.4. The position angle – conventions

Contrary to BCW91 and HA2001 we assume that the position angle ψ increases *counterclockwise* on the sky, ie. we follow the usual astronomical convention (Damour & Taylor 1992; Everett & Weisberg 2001, hereafter EW2001). HA2001 studied the influence of rotational effects and magnetospheric currents on the shape of the position angle curve and found that some of these effects result in vertical shifts of the entire PA curve. Since the conventional position angle ψ corresponds to the negative of the position angle ψ_{HA} considered by HA2001 (ie. $\psi = -\psi_{HA}$), the rotationally-induced vertical shifts of the conventional PA curve $\psi(\phi)$ occur in the opposite direction than the shifts of the curve $\psi_{HA}(\phi)$ described by

HA2001. In particular, the aberration-induced decrease (or downward shift) of ψ_{HA} found by HA2001 for $\zeta < 90°$ corresponds to the upward shift of the conventional PA curve $\psi(\phi)$.

In figures with model results we present position angle curves only for viewing angles $\zeta_{\mathrm{obs}} \leq 90°$, since the position angle is antisymmetric with respect to the rotational equator. Thus, an observer located at $\zeta'_{\mathrm{obs}} = 180° - \zeta_{\mathrm{obs}}$ records the PA curve $\psi'(\phi)$ which is a mirror image (with respect to $\psi = 0$) of the PA curve $\psi(\phi)$ recorded by an observer located at ζ_{obs}. More precisely, the mirror image is shifted horizontally in phase by half the rotation period, ie. $\psi'(\phi) = -\psi(\phi + \pi)$.

The modelled position angle curves are symmetric with respect to the transformation $\alpha \to \pi - \alpha$, because the velocity of electrons (used to determine $\vec{a} \parallel \vec{E}_{\mathrm{w}}$) is assumed to be directed outwards in both magnetic hemispheres, so that the information about the direction of the positive dipole axis $(+\vec{\mu})$ is lost. The transformation only shifts the position angle curves horizontally by half the rotation period: $\psi'(\phi) = \psi(\phi + \pi)$. The sign of ψ is not affected (no mirror reflection). Obviously, unlike in the case of the *modelled* position angle curve, the horizontal shift by half the rotation period cannot be recognized in the *observed* PA curve (ie. it does not allow us to discern between α and $\pi - \alpha$) because the assignment of the zero phase to the observed PA curve is arbitrary and the pulse profile undergoes the same shift as the PA curve (ie. $I'(\phi) = I(\phi + \pi)$). The behaviour of the position angle curve under the reflections of the dipole moment $\vec{\mu}$ and the observer's position with respect to the rotational equator is summarized in Table 1.

Thanks to the symmetries presented in Table 1, a fit of the modelled position angle curve to the high-energy polarization data enables unambiguous determination of the viewing angle ζ_{obs}, but *does not* allow us to discern between α and $\pi - \alpha$. The value of ζ_{obs} usually cannot be uniquely derived from fitting the PA curves to *radio* data (eg. EW2001), because the latter are usually limited to a very narrow range of rotational phase. Pulsar profiles at high photon energies usually have significantly larger duty cycles than at the radio frequencies, which should remove the problem of determining ζ_{obs} as soon as high quality polarization data and reliable models of position angle curves at high energy bands are at hand.[2]

---

[2]Our conclusion, that the fit of the position angle curve makes it possible to unambiguously determine the value of ζ_{obs} but not α, may seem to be contradicted by the wording of EW2001, who claim that the fit enables the unambiguous determination of "α". Actually, however, the apparent disagreement results from different definitions of α. In this paper we assume that α is the angle between the positive rotation axis (pointing in the direction of $\vec{\Omega}$) and the magnetic moment of the dipole $\vec{\mu}$ (pointing toward the magnetic north). EW2001 use α_{EW} defined as the angle between $\vec{\Omega}$ and the *observable magnetic pole*, regardless of whether the pole is magnetically northern or southern. Obviously, the value of α_{EW} defined in this way, along with the value of $(\zeta_{\mathrm{obs}} - \alpha_{\mathrm{EW}})$ which EW2001 derive from their fits, provide unambiguous information about

Also because of the symmetries presented in Table 1, the position angle curves calculated for the clockwise definition of position angle (eg. those shown in figures in HA2001) can be considered as the position angle curves for the standard (ie. counterclockwise) definition of ψ, but for viewing angles $\zeta_{\text{obs}} = \pi - \zeta_{\text{obs}}^{\text{orig}}$ and the dipole inclinations $\alpha = \pi - \alpha^{\text{orig}}$, where the angles with the superscript 'orig' are those given in the published works with the clockwise definition of the position angle (cf. Table 1, last row).

Finally, we recall that when calculating the modelled position angle we assume the projection of the vector $\vec{\Omega}$ on the plane of the sky as the reference direction corresponding to $\psi = 0$. The position angle determined from observations is conventionally measured from the northern direction through east. To compare the absolute values of the modelled position angle with the data it is therefore necessary to add to the modelled values the observed position angle of the pulsar rotation axis. Moreover, we assumed that the polarization direction is *parallel* to the local acceleration vector $\vec{a}$. If the actual polarization direction is *perpendicular* to $\vec{a}$ (as in the case of the radio emission from the Vela pulsar, Lai et al. 2001; Helfand et al. 2001; Radhakrishnan & Deshpande 2001) an additional 90° shift must be applied to the modelled position angle curve, before absolute comparison can be performed.

3. Results

3.1. The two-pole caustic model

3.1.1. Lightcurves

In the two-pole caustic model (Dyks & Rudak 2003) pulsations result from rotation of a dipole with roughly uniform photon emission along the entire length of the last open magnetic field lines. For most dipole inclinations two strong caustics form on the trailing side of open field line cones related to both polar caps. They can be seen in Fig. 4, which presents projection of magnetic field lines onto the $(\phi, \zeta_{\text{obs}})$ space, where ϕ is the phase of the pulse, and ζ_{obs} is the angle between the rotation axis and the observer's line of sight. The pattern was calculated for $\alpha = 60°$, $P_{\text{rot}} = 0.033$ s, and for 90 magnetic field lines with their footprints spaced uniformly *along the rim* of the polar cap as shown in Fig. 3 (ie. non-uniformly in ϕ_{m}). The blank deformed ovals are polar caps and the two trailing caustics can

---

the location of the observer (ie. about ζ_{obs}) rather than about the direction of $+\vec{\mu}$. The angle $\alpha \equiv \angle(+\vec{\Omega}, +\vec{\mu})$ cannot be uniquely determined from the fits of modelled position angle curves to pulsar data, regardless of the frequency of the observation (ie. radio or high-energy). The fits provide us only with $\sin\alpha$, ie. do not allow to discern between α and $\pi - \alpha$.

be identified as the dark arches spanning a large range of ζ_{obs} near the phases $\phi = 0.05$ and 0.55.

The formation of the trailing caustics was explained already by Morini (1983) (see his fig. 2): an increase in photon emission altitude along a trailing magnetic field line results in a phase delay/shift which is almost completely compensated by effects of aberration and time of flight. Therefore, photons emitted within a broad range of altitudes are piled up at roughly the same phase. On the leading part of the open field line cones the same special relativity effects produce the opposite effect: photons are spread out over a large range of ϕ, forward in phase.

Morini's model assumed that an observer views caustic emission from only one pole. Dyks & Rudak (2003) have introduced a model where the observer sees caustic emission from both poles. Since for observer positions ζ_{obs} departing from the rotational equator the two trailing caustics approach each other, observers located at $90° - \alpha \lesssim \zeta_{obs} \lesssim 90° + \alpha$ (and $\zeta_{obs} \neq 90°$) will detect double peaked pulse profiles with the peak separation $\Delta^{peak} \neq 0.5$. Observers located at small angles with respect to the rotation axis ($90° + \alpha \lesssim \zeta_{obs} \lesssim 90° - \alpha$) will detect single pulse profiles.

As can be seen in Figs. 4 and 5 these conclusions, drawn by Dyks & Rudak (2003) based on results for a static shape dipole, prevail in the retarded dipole case. Fig. 5 presents radiation characteristics predicted by the two-pole caustic model for a pulsar with $\alpha = 60°$, observed at nine different angles ζ_{obs}. The other parameters of the model were: $r_{ovc} = 1$, $\rho_{max} = 0.75 R_{lc}$, $r_{max} = R_{lc}$, and $P_{rot} = 0.033$ s. The figure consists of 9 three-panel frames, corresponding to the 9 different viewing angles ζ_{obs}, shown in the upper right corner of upper panels. Each frame presents a lightcurve (upper panel), a position angle curve (dots, often merging into a thick solid line, middle panel), and a degree of polarization (thick solid line, lower panel). In the middle and in the lower panel, the lightcurve from the upper panel is overplotted for a reference (thick grey line).

For large viewing angles ($|90° - \zeta_{obs}| \lesssim \alpha$) two peaks (separated by $0.35 - 0.5$) due to crossing the trailing caustics can be easily identified in the upper panels of Fig. 5. The leading peak (P1) is located close to $\phi = 0.1$, ie. it lags by 0.1 the phase zero, at which an observer's line of sight approaches most closely the dipole axis. This is consistent with the relative positions of gamma-ray and radio peaks observed for the Vela pulsar and PSR B1951+32 (Fierro 1995), since the observed radio peaks are commonly interpreted in terms of a narrow cone of radiation aligned with the magnetic dipole axis. The Crab pulsar is a special case with a very complicated radio pulse morfology (Moffet & Hankins 1999). However, polarization properties of the Crab suggest that the closest approach to the dipole axis also occurs at the phase preceding by ~ 0.1 the leading gamma-ray peak (Moffet & Hankins 1999), which

again agrees with the prediction of the two-pole caustic model. In section 3.4 we show that positions of the main features of the Crab's radio profile (a precursor, a main peak, and an interpulse) can be interpreted within the two-pole caustic model. In the case of the Geminga pulsar no stable radio profile has been determined so far (eg. Malofeev & Malov 2000) and a gamma-ray lighcurve features two peaks separated by 0.5. The two-pole caustic model pedicts $\Delta^{\mathrm{peak}} = 0.5$ for $\alpha \simeq 90°$ and any ζ_{obs}, or for $\zeta_{\mathrm{obs}} \simeq 90°$ and any α (Fig. 5i). This interpretation contradicts models of Geminga's radio emission which require nearly aligned geometry (small α *and* ζ_{obs}, Gil et al. 1998; Malofeev 1998) but may explain why Geminga's radio flux is so small, since the line of sight does not approach near to the pole..

Relative intensities and widths of the leading peak (P1) and the trailing peak (P2) (Fig. 5) are far from those observed in gamma rays (Kanbach 1999, Thompson 2001), however, we show below that these characteristics are very sensitive to the magnetic field structure close to the light cylinder, and to other model parameters. Apart from the two peaks, there are a few more features (marked with the letters O, N, and S in Fig. 5) present in the lightcurves. Their origin is the following: Features marked with O arise due to partial overlap of two emission patterns from each of the polar caps, and can be easily understood by inspecting Fig 4. Features marked with N (Fig. 5e, f) are produced when the line of sight crosses emission from the bunch of lines emerging from the notch part of the polar cap rim. In spite of the fact that the spatial spread of the last open magnetic field lines at high-altitudes is the largest just for the lines anchored at the notch, projections of these widely spreaded "notch lines" on the $(\phi, \zeta_{\mathrm{obs}})$ plane overlap. This "notch bunch" of magnetic field lines can be identified in Fig. 4 in regions which precede the polar caps in phase. Had the notch been not present in the polar cap, the N-features would disappear. Features marked with S (small step-like drops in emission level, Fig. 5g, h, i) are produced because high altitude spread of the last open lines changes discontinuously at the second critical point C2 at the polar cap rim (even though the lines' footprints are spreaded uniformly along the polar cap rim). This slight jump in the lines' spread can also be noticed in Fig. 4.
Further discussion of lightcurves predicted by the two-pole caustic model is included in the following subsections.

3.1.2.   Polarization

Polarization data on pulsars are limited to radio frequencies, with the only exception being the Crab pulsar, for which polarization data in near-infrared, visible, and ultraviolet light are available (Jones et al. 1981; Smith et al. 1988; Graham-Smith et al. 1996; Romani et al. 2001; Kanbach et al. 2003). X-ray and gamma-ray experiments will be able to measure

polarization of bright pulsars in the near future (eg. Bloser at al. 2003).

The variations of position angle observed for the Crab at optical (Fig. 6; Kanbach et al. 2003) differ from those observed at radio wavelengths (Moffet & Hankins 1999). There may be two reasons for such difference: 1) Radio emission at fixed frequency is usually interpreted as coming from a limited range of altitude, contrary to the high energy emission (including optical) which is believed to originate from a wide range of altitudes, at least in the two-pole caustic, and in the outer gap model. Therefore, below we will compare predictions of these models with the highest energy polarization data which are available, ie. with the optical data on the Crab pulsar (UV polarization data (Graham-Smith et al. 1996) are not as good in quality as the optical data). 2) Position angle may depend on photon energy. This is possible because a directional distribution of radiation emitted by a single electron depends on the electron's energy and, therefore, on a characteristic frequency of the emitted radiation. A convolution of these single-electron radiation patterns with a spatial distribution of electrons may then result in the frequency-dependence of position angle (Chen et al. 1996). This effect certainly is worth closer investigation but is beyond the scope of the present geometrical approach.[3]

Perhaps the most striking feature of optical emission from the Crab is the fixed value of position angle within low-intensity phase intervals (Fig. 6, Kanbach et al. 2003). Astonishingly, the value is the same for the bridge, and for the off-pulse region. This feature cannot be understood within any model which connects the position angle directly to the geometry of the rotating dipole within the light cylinder radius. We comment on the possible origin of this constant component in Section 4 (Conclusions).

The constancy of ψ suggests that the optical emission from the Crab pulsar is a superposition of two components: 1) a pulsed component with highly variable position angle and polarization degree, with the latter being very small (~ 2 %) just behind the peaks' maxima; 2) a constant intensity component with fixed position angle ($\sim 123°$) and relatively high polarization degree (~ 40 %).

Such a superposition of two polarized sources may easily produce artifact features in the position angle curve and in the polarization degree curve, especially when the intensities of

---

[3]Although we largely ignore the spectral dependence of polarization characteristics, we discern between the coherent radio emission (with the well established phenomenology) and the high-energy emission which in general is spatially and spectrally separated from the radio. We use the term "high-energy" for non-thermal X-rays, gamma-rays, and for optical emission, provided the latter has the same origin as gamma-rays. This is justfied in the case of the Crab pulsar, for which both optical and gamma-ray emission occur at the same phases and have spectra which connect smoothly.

the polarized part of the radiation for both these components are comparable. Unfortunately, the latter condition seems to be the case for the Crab: although the intensity at the leading peak exceeds by a factor of ~ 100 the intensity of the constant component, the latter seems to be highly polarized ($P \sim 35$ %), whereas the polarization degree of the pulsed component drops to ~ 2 % at the leading peak. Therefore, even at the maximum of the leading peak, the polarized intensity of the pulsed component exceeds the polarized intensity of the constant component only by a factor of $3 - 5$. This makes extracting the pulsed signal from the total data a crucial task.

The polarization properties of the pulsed signal are presented by Kellner (2002), who has subtracted from the total signal a constant component with $\psi = 123°$, $P = 33$ %, and $I = 1.24$ % of the maximum intensity at the first peak. A result of such a manipulation is also shown in the right column of Fig. 6 (this paper): the fast swings of position angle at both peaks extend over much larger range of ψ, and the constancy of ψ beyond the peaks disappears. The polarization degree assumes low values ($P \lesssim 10$ %) at all phases dominated by the pulsed signal. The value of P is especially low ($P \sim 2$ %) within the phase intervals trailing both peaks.

Dyks & Rudak (2003) suggested that the minima in polarization percentage P could naturally result from the caustic nature of the peaks: superposition of emission from different altitudes (ie. with different position angles), which produces the peaks, could ensure both the decrease in P and the fast swings of ψ. This phenomenon was expected for both the two-pole caustic and the outer gap model.

As can be seen in Fig. 5 (middle panels, $\zeta_{\mathrm{obs}} \lesssim 70°$) the two-pole caustic model does predict fast changes of ψ at the leading peak (P1), close to phase 0.1. The change of ψ at P1 is faster on the trailing side of the peak, than on the leading side, in agreement with the Crab data. In the case presented in Fig. 5, ie. for photon emission limited to the last open magnetic field lines ($r_{\mathrm{ovc}} = 1$), the two-pole caustic model does not predict the fast increase of ψ at the trailing peak (P2) located near the phase $\phi = 0.5$. Just behind P2, the position angle changes discontinuously by a few tens of degrees, when the line of sight starts to sample emission from the other magnetic pole.

The fast increase of ψ at the leading peak P1 lags in phase the near-pole, radio-like fast swing of position angle at the phase zero (cf. Fig. 5, middle panels). The radio-like swing near phase zero has the same origin as the swings commonly observed at radio frequencies, ie. it results from the line of sight passing nearby the magnetic pole. It differs from the radio swings only in that it is produced by radiation originating from various altitudes. Like the radio swings, the swing near the magnetic pole at $\phi = 0$ changes sign for the line of sight passing on opposite sides of the magnetic pole, ie. it depends on the sign of the impact angle

$\beta = \zeta_{\mathrm{obs}} - \alpha$ (compare middle panels of frames d and g in Fig. 5). The fast change of ψ which occurs at the leading caustic peak, however, does not depend on the sign of the impact angle. At P1 the position angle ψ always increases (for $\zeta_{\mathrm{obs}} < 90°$), regardless of whether the line of sight passes above, or below the magnetic pole. Thus, the caustic model predicts that the Crab pulsar is viewed at the angle $\zeta_{\mathrm{obs}} < 90°$. (For $\zeta_{\mathrm{obs}} > 90°$ the PA would decrease at the leading peak, cf. Section 2.4).

In the regions where the caustic pile up is most pronounced (see Fig. 4) the geometry of different field lines which contribute at the same phase is very similar and, therefore, there is no significant depolarization at the peaks (Fig. 5, lower panels). The only considerable drops in P occur at the overlap regions (marked with O in Fig. 5). The minima caused by the overlap often occur at (or just behind) the peaks, in agreement with observations.

We find that under the present assumptions (in particular in the case of the photon emission constrained only to the last open field lines) the two-pole caustic model is not able to *exactly* reproduce the Crab polarization data, for any model parameters. Fig. 7 presents results for another type of calculation – with electron density distribution slightly smeared around the polar cap rim (a Gaussian with $\sigma = 0.025$, centered at the rim, between $r_{\mathrm{ovc}}^{\min} = 0.95$, $r_{\mathrm{ovc}}^{\max} = 1.05$). It has been obtained for $\alpha = 70°$, $\zeta = 50°$, $\rho_{\max} = 0.8 R_{\mathrm{lc}}$, $r_{\max} = R_{\mathrm{lc}}$, and $P_{\mathrm{rot}} = 0.033$ s.

The spread in electron density is responsible for comparable intensity of both peaks in the lightcurve (Fig. 7, upper panel). This is because in the case $r_{\mathrm{ovc}} = 1$ (Fig. 5) the leading peak is much broader than the trailing peak. Photon emission from magnetic field line cones with different, fixed r_{ovc} produces peaks at slightly different phases. Broad leading peaks for different cones overlap in phase, whereas narrow trailing peaks do not sum up in phase. Another new feature caused by the surface density spread is the fast increase in position angle *behind* the trailing peak (Fig. 7, middle panel). Although resembling the fast swing at P2 observed in the optical Crab data, the modelled swing does not coincide in phase with P2, and occurs within the low-intensity trailing wing of P2. Moreover, at the leading peak the modelled position angle ψ spans a different range of values ($50° - 180°$) than at the trailing wing of P2 ($-50° - 90°$). The observed range of values assumed by the position angle at the leading peak of the Crab's optical profile is roughly the same as the one observed at the trailing peak (Fig. 6). The last effect of the density spread is the noticeable decrease in the degree of polarization near the peaks (Fig. 7, bottom panel). The narrow dip in polarization degree which almost coincides with P1 (located near $\phi = 0.1$) is caused by superposition of emission from nearby magnetic field lines (with slightly different r_{ovc}) emerging from the same, northern magnetic pole. Likewise, the minimum in P at the phase $\phi = 0.48$ which slightly precedes the trailing peak originates from the superposition

of emission from nearby magnetic field lines, all of which emerge from the same, southern magnetic pole. Although the superposition of emission from adjacent magnetic field lines occurs at any phase ϕ, it results in the drop in P only at the peaks. This indicates that the caustic effects at the peaks are crucial for producing this minima in P. The other minima in P, following both peaks result from superposition of radiation patterns from the different magnetic hemispheres. Their shape and depth depends sensitively on the parameters ρ_{max} and r_{max}, since including the near-R_{lc} region greatly increases the area on the (ϕ, ζ_{obs}) plane within which the two radiation patterns from the opposite magnetic hemispheres overlap. Therefore, the degree of polarization may provide a good diagnostic of pulse profiles with overlapping emission from regions widely separated in space. There is a large variety of polarization degree curves which can be produced by the two-pole caustic model, given the large number of combinations of parametrs α, ζ_{obs}, ρ_{max}, r_{max}. We find that in general, however, both the leading and the trailing peak are followed by a minimum in polarization degree, which is in qualitative agreement with the optical data on the Crab pulsar (Fig. 6, bottom right panel).

3.1.3. Static shape dipole

A rigidly rotating static shape dipole is worth consideration for two reasons: 1) calculations are much simpler for this field structure; 2) by comparison of results for the static dipole with those for the retarded dipole one can assess the importance of the near-R_{lc} distortions of magnetic field for predicted radiation characteristics.

Let us first discuss the static shape dipole with photon emission from "actual" last open magnetic field lines, ie. those which are tangent to the light cylinder and emerge from the oval-shape polar cap rim, drawn with the dashed line in Fig. 1. We find pronounced differences between radiation characteristics calculated for this case and for the above-described retarded case. In the static dipole case, and for moderate inclination angles ($\alpha \sim 60°$), the radiation pattern from a single magnetic pole tends to be projected mostly within one rotational hemisphere – ie. when projected on the (ϕ, ζ_{obs}) plane of Fig. 4 it would mostly occupy only its upper half (or lower half, for the opposite pole). There is a very small range of viewing angles close to the rotational equator ($\zeta_{obs} \gtrsim 80°$), for which the pulse profiles are double-peaked and resemble those shown in Fig. 5. It is difficult to obtain peak separation much different from 0.5 and most viewing angles result in single peak lightcurves. These modifications take place because the last open magnetic field lines of the static shape dipole emerge from the oval-shape polar cap rim – squeezed in the direction of rotational colatitude θ (Fig. 1, dashed line). Magnetic field lines anchored at the oval rim close to $\phi_m = 0$ or $180°$

extend in the θ direction much less than than those anchored at the same ϕ_{m} in the retarded dipole case (cf. the shapes of polar cap rim for these two cases, Fig. 1).

We conclude that the rotational distortions of the near-R_{lc} magnetic field structure have a large influence on the resulting radiation characteristics. We emphasize that the distortions of the pulsar radiation pattern are effects of *lower* order than β_{cor}^2, where β_{cor} is a local corotation velocity in units of the speed of light. Eg. the average radius of the polar cap shown in Fig. 1 changes by $\sim 10\ \%$ (or, by $\sim 8 \cdot 10^{-3}$ rad), whereas $\beta_{\mathrm{cor}}^2 = 2 \cdot 10^{-5}$ for $P_{\mathrm{rot}} = 0.033$ s, $R_{\mathrm{ns}} = 10^6$ cm, and a distance of the polar cap from the rotational axis $R_{\mathrm{ns}} \sin \alpha \simeq 7 \cdot 10^5$ cm. In fact, the rotational distortion of the radiation pattern is even larger than β_{cor} which is equal to $4.5 \cdot 10^{-3}$ at the polar cap shown in Fig. 1. Some geometrical models of radio properties of pulsars (eg. Blaskiewicz et al. 1991; Gangadhara & Gupta 2001) fully rely on symmetry of the open field line cone with respect to the $(\vec{\Omega}, \vec{\mu})$ plane. The rotational distortions of the magnetic field are neglected in the models, and the asymmetry of radio pulse profiles with respect to some fiducial features (eg. the center of position angle curve, Blaskiewicz et al. 1991, or the position of the core component, Gangadhara & Gupta 2001) is interpreted purely in terms of aberration and finite propagation time of radio waves. The strong, rotational distortions of the open field line region, visible in Fig. 1, indicate that the rotationally induced sweep-back of magnetic field lines should have been taken into account in these models.

The most convenient calculation of pulsar radiation characteristics is based on the static shape dipole geometry, *and* it employs the standard circular polar cap rim of radius r_{pc} as the position of footprints of the "last open" magnetic field lines at the star surface. Contrary to the above discussed case of the oval cap, a calculation of this type approximates very well the lightcurves obtained for the retarded dipole, a fact emphasized by RY95. This can be easily understood: as can be seen in Fig. 1 the circular polar cap approximates the retarded polar cap better than the actual, oval-shape polar cap for the static dipole case (cf. thin solid, thick solid, and dashed polar cap rims in Fig. 1).

Fig. 8 presents a lightcurve (a), a position angle curve (b), and a degree of polarization (c) for the static dipole case with the circular polar cap. Parameters used in the calculation were the same as in Fig. 7. Note the resemblance of the lightcurve and the polarization characteristics to those one for the retarded dipole case (Fig. 7).

Reproducing the lightcurve of the Crab pulsar is a little bit problematic for the two-pole caustic model, because it often predicts a bump of emission at phases following the first peak (Fig. 5c-g, Fig. 7a). This feature has a twofold origin: 1) in part it is produced by an overlap of emission patterns from two poles; 2) it is a trailing wing of a peak which would form very close to the light cylinder ($\rho > 0.8 R_{\mathrm{lc}}$) at the leading side of the open field line cone.

This is the peak which is interpreted as the leading peak in the outer gap model (RY95; CRZ2000). It usually slightly lags the first peak of the two-pole caustic model, although the actual value of the phase lag depends on viewing geometry. In the lightcurves predicted by the two-pole caustic model the peak appears only when high-altitude emission is included. Had the photon emissivity declined with altitude above some $r \gtrsim 0.5R_{\rm lc}$, the feature would be much less pronounced or would disappear.

Interestingly, however, such a feature is present in the gamma ray lightcurve of the Vela pulsar (Grenier et al. 1988; Kanbach et al. 1994; Thompson 2001). Fig. 9 shows the Vela lightcurves for photon energy range of $2.8 - 10$ GeV (a) and for the entire energy band of EGRET (30 MeV – 10 GeV, panel b). A lightcurve predicted by the two-pole caustic model is shown in panel c. Note that the shape of the broad-band lightcurve is very well reproduced by the two-pole caustic model: the leading peak is narrower than the trailing peak, which connects smoothly with the bridge emission. The leading peak does not connect smoothly with the bridge, and is followed by the "postcursor bump". These features result naturally from the two-pole caustic model, since it predicts that the trailing peak, the bridge emission, and the "postcursor bump" arise from sampling a single, continuous radiation pattern from one magnetic pole (cf. Fig. 4). The leading peak and the offpulse emission are produced by sampling an emission pattern from the opposite magnetic pole. Such a two-component decomposition of the Vela lightcurve is confirmed by the lightcurve observed within higher energy range between 2.8 and 10 GeV (Fig. 9a), where the trailing peak remains smoothly connected to the bridge, whereas the leading peak seems to present a separate entity. We emphasize that our interpretation of the gamma-ray lightcurve of the Vela pulsar (with $\alpha \simeq 70°$ and $\zeta_{\rm obs} \simeq 60 - 65°$) is in very good agreement with a geometrical model of X-ray arcs surrounding the pulsar in Chandra images (Radhakrishnan & Deshpande 2001 – the model; Pavlov et al. 2000 and Helfand et al. 2001 – observations). In Fig. 4 of Dyks & Rudak (2003) we chose $\alpha = 70°$ and $\zeta_{\rm obs} = 61°$ to reproduce the observed peak separation of ~ 0.43 while keeping the difference $\alpha - \zeta_{\rm obs}$ smaller than $\sim 10°$ to ensure the close approach to the narrow radio beam centered at the dipole axis. Given the relatively weak sensitivity of the peak locations to α and $\zeta_{\rm obs}$ (eg. cf. Fig 3 in RY95) the inferred values of these parameters have accuracy of a few degrees. Radhakrishnan & Deshpande (2001) infer similar values of $\alpha = 71°$ and $\zeta_{\rm obs} = 65°$ from their interpretation of the X-ray arcs, ie. on a completely different basis than our. We have used their values to calculate the two-pole caustic model lightcurve in Fig. 9c. The closer approach to the dipole axis ($|\zeta_{\rm obs} - \alpha| = 6°$ in comparison with $9°$ in Dyks & Rudak 2003) is in excellent agreement with the fits of the position angle swing to the radio data (Krishnamohan & Downs 1983; Johnston et al. 2001).

The model results in Figs. 8 and 9c have been calculated for the circular-cap approximation and for the static-shape dipole, which are also assumed in Section 3.3 and in Fig. 11.

All the other results presented in this paper have been obtained for the retarded dipole with the distorted shape of the polar cap.

3.2. Outer gap model

In this section we decribe predictions of the most popular version of the outer gap (OG) model described eg. in RY95 and CRZ2000. This version assumes that the outer gap extends from the null charge surface up to the light cylinder not only in the $(\vec{\Omega}, \vec{\mu})$ plane, and that radiation emitted outward dominates. Other versions of the OG model (Cheng et al. 1986; Chen et al. 1996) are not treated here.

Although the traditional geometry of the outer gap has recently been questioned (Hirotani & Shibata 2001) the model maintains its great popularity because it naturally explains some features of observed lightcurves (in particular the relative positions of gamma-ray and radio peaks, Chiang & Romani 1992; RY95) and it *seemed* to produce fast swings of position angle at both peaks (RY95).

Our calculations confirm the success of the OG model in reproducing the relative phases of radio and gamma ray peaks; however, our polarization results for this model do not agree with the data and contradict previous results presented by RY95. Moreover, the ability of the model to reproduce lightcurves fully relies on including photon emission from the very vicinity of the light cylinder ($0.8R_{\mathrm{lc}} \lesssim \rho \lesssim R_{\mathrm{lc}}$), where the vacuum magnetic field dipole approximation is not valid.

In the outer gap model, the position of magnetic field line footprints at the star surface becomes a crucial parameter. For the simplest choice: $r_{\mathrm{ovc}} = 1$ (polar cap rim) the observed gamma-ray lightcurves cannot be well reproduced and, therefore, it is necessary to assume $r_{\mathrm{ovc}} < 1$ (usually close to 0.9).

Fig. 10 presents lightcurves and polarization calculated for the outer gap model with $\alpha = 65°$, $\rho_{\mathrm{max}} = 0.999R_{\mathrm{lc}}$, and $r_{\mathrm{max}} = 1.7R_{\mathrm{lc}}$. A gaussian spread in electron density has been assumed in this calculation with $r_{\mathrm{ovc}}^0 = 0.9$, $\sigma = 0.025$ and r_{ovc} ranging between 0.85 and 0.95. The results are presented in the same way as in Fig. 5. For large viewing angles ζ_{obs} (Fig. 10g, h, i) the well known double peak shape of lightcurves obtained by RY95 and CRZ2000 can be recognized.

A relatively fast increase of the position angle appears at the trailing peak (Fig. 10e, f, g, h). At the leading peak, however, either the fast changes of PA do not occur (Fig. 10g, h, i) or they occur in the opposite direction than at the trailing peak (Fig. 10e, f). The same

behaviour also takes place for larger dipole inclinations α, including $\alpha \gtrsim 70°$ for which RY95 found fast changes of ψ at both peaks (for $\zeta_{\rm obs} \lesssim 70°$).

Our polarization results for the outer gap model cannot reproduce those published by RY95. We have checked if the disagreement results from different calculation methods – RY95 assumed that the polarization direction $\vec{E}_{\rm w}$ is parallel to the local radius of curvature of magnetic field lines $\vec{\rho}_{\rm curv}$, whereas we present the results for $\vec{E}_{\rm w} \parallel \vec{a}$. We find that for $\vec{E}_{\rm w} \parallel \vec{\rho}_{\rm curv}$ the fast changes of PA do occur in the parameter range suggested by RY95 ($\alpha \gtrsim 70°$, $\zeta_{\rm obs} \lesssim 70°$), however, only at the leading peak. Moreover, we find that even the swing at the leading peak is problematic, since it occurs for photon emission along the magnetic field lines emerging very close to the polar cap rim ($r_{\rm ovc} \gtrsim 0.9$) whereas the good looking lightcurves are produced for ($r_{\rm ovc} \lesssim 0.9$). Although we used the same calculation method, the same model parameters as in RY95 and we densely sampled a large range of model parameters not specified in RY95, we were not able to reproduce the result shown in fig. 5 of RY95.[4]

A serious disadvantage of the outer gap model is that the swing at the leading peak (as well as the peak itself – see below) is formed very close to the light cylinder – at $0.8 R_{\rm lc} \lesssim \rho \lesssim R_{\rm lc}$ (and $r \gtrsim R_{\rm lc}$), where the geometry of the magnetic field is not known. In calculations which discard the near-$R_{\rm lc}$ emission ($\rho_{\rm max} = 0.8 R_{\rm lc}$), the leading peak is missing.

3.3. Polar cap model

In the polar cap model (Ruderman & Sutherland 1975; Arons & Scharlemann 1979) acceleration takes place close to the star surface (at altitudes $h \lesssim r_{\rm pc}$ or $h \lesssim R_{\rm ns}$, depending on the boundary conditions at the surface), which implies a very narrow beam for gamma-ray, and radio emission. Therefore, the polar cap model is able to reproduce the widely separated double peaks in pulsar lightcurves only if the rotation axis, the magnetic dipole axis, and the observer's line of sight are nearly aligned (Lyne & Manchester 1988; Daugherty & Harding 1994; Dyks & Rudak 2000). With the nearly aligned geometry included, the model is able to reproduce phase-resolved high-energy spectra of the Vela pulsar (Daugherty & Harding 1996) as well as a fading of the leading peak at the high-energy spectral cutoff (Dyks & Rudak 2002). A long list of advantages of the polar cap model over the other models can be found in Baring (2001).

---

[4]Unfortunately, RY95 do not specify what value of w was used in their calculation. We were not able to reproduce their result for any value of w. We argue that either their result is incorrect, or it requires a very precise adjustment of model parameters. Certainly, it is not a natural prediction of the outer gap model.

Slot gap geometry somewhat eases the requirement of alignment, but small inclination angles are still necessary (Muslimov & Harding 2003a). This is a real problem for the polar cap model, since there is no statistical evidence for more frequent occurence of small inclinations angles among young pulsars (Lyne & Manchester 1988; Blaskiewicz et al. 1991). The polar cap model predicts that the nearly aligned rotators are about one order of magnitude brighter gamma-ray sources than pulsars with larger dipole inclinations (Dyks 2002). This is because in the nearly aligned geometry, the observer's line of sight samples the high intensity polar cap beam of radiation for a much longer fraction of the rotation period than in the case of large dipole inclinations. Although this implies higher probability of detection for the nearly aligned rotators, X-ray and radio studies of particular cases contradict the nearly aligned geometry (eg. Crab, Hester et al. 1995, and Vela, Krishnamohan & Downs 1983; Radhakrishnan & Deshpande 2001). Moreover, although the near alignment ensures large separations between the two gamma-ray peaks, it does not explain why so many gamma-ray pulsars (~ 50 %) have Δ^{peak} in the narrow range between 0.4 and 0.5. Apparently, the polar cap model is not able to explain the observed shape of gamma-ray lightcurves naturally.

Moreover, the polar cap model predicts that the only fast swing in position angle ψ should occur midway between the gamma-ray peaks – not at the phase of the gamma-ray peaks. A typical shape of the position angle curve predicted by the polar cap model is shown in Fig. 11b. It has been calculated for the static shape dipole geometry of the magnetic field with the circular polar cap. The following, simplified emission region was assumed to calculate the PA curve: For $r_{\mathrm{ovc}} < 1$ (ie. inner regions of the open field line tube) the high-energy radiation was assumed to be emitted along all (open) field lines at a fixed radial distance $r = 3R_{\mathrm{ns}}$. For $r_{\mathrm{ovc}} = 1$ (the last open field lines) the emission originated from all radial distances exceeding $3R_{\mathrm{ns}}$. This choice of the emission region is an effort to simplify the complex emission pattern of the polar cap model: At any rotational phase, an observer detects radiation from many different altitudes and from many different magnetic field lines. However, as long as the line of sight cuts through the acceleration region located at $r = 3R_{\mathrm{ns}}$ (which takes place for $|\phi| \lesssim 0.2$ for the viewing parameters used in Fig. 11) the high-energy radiation from the accelerator should dominate the detected signal. For $|\phi| \gtrsim 0.2$ the line of sight no longer cuts through the accelerator (limited to the open field lines), and, therefore, the received radiation should be dominated by emission from the last open magnetic field lines, where the model assumes an enhanced electron density to produce pronounced peaks.

The central parts of the PA curve, due to the photon emission from the fixed altitude, are marked in Fig. 11 with dots. The fast swing of ψ visible in Fig. 11 near $\phi = 0$ has the same origin as the swings observed at radio frequencies, ie. it results from the line of sight passing nearby the magnetic pole. Contrary to the prediction of the polar cap model, the well established interpretation of position angle swings at radio frequencies implies that the

swing should occur at the phase of a radio peak. In the case of pulsars with gamma-ray profiles with two widely separated peaks (Crab, Vela, B1951+32) the phase of the radio swing precedes by ~ 0.1 the leading gamma-ray peak. If the standard interpretation of radio properties applies to gamma-ray pulsars (and, except from the Crab case, there is no reason for which it should not apply), it contradicts the polar cap model unless the radio peaks are leading edge cone emission.

As described in BCW91 and HA2001, the special relativity effects associated with the star's rotation influence the position of the PA curve. Two effects of rotation can be discerned in Fig. 11: 1) the delay of the PA center (located at $\phi \simeq 2r/R_{\rm lc}$) with respect to the profile center (at $-2r/R_{\rm lc}$) discovered by BCW91, and 2) the upward shift of the PA curve by $(10/3)(r/R_{\rm lc})\cos\alpha$ found by HA2001 (the *downward* shift, as originally described by HA2001, takes place for $\zeta_{\rm obs} > 90°$, see the discussion in Section 2.4). The presence of these effects in the modelled PA curve confirms the correctness of our numerical code. Since in our geometrical approach a depolarization can result only from overlaps of emission from different altitudes, for the polar cap model it remains constant at the "intrinsic" level of 80 % for any phase ψ (not shown in Fig. 11).

As long as the low altitude high-energy emission and the nearly aligned geometry is considered, the caustic effects are not important for the polar cap model. However, the effects become important if lower-energy emission (eg. optical, X-ray) from high-altitudes and larger dipole inclinations are considered (an example of such a case is the polar cap model of Morini 1983). The original polar cap model where acceleration is limited by electromagnetic cascades at low altitude induced mostly by curvature radiation, predicts lightcurves very similar to those for the two-pole caustic model (Fig. 5) in two cases: 1) in the off-beam viewing geometry; 2) for any viewing geometry at photon energies smaller than ~ 100 MeV and only within photon energy range dominated by curvature radiation (not by the synchrotron radiation). In addition to the two caustic peaks, the lightcurves often possess an additional peak near phase zero, caused by enhanced photon emission near the star surface.

These lightcurves, however, could be observed only at photon energies lower than ~ 100 MeV, which is the energy of the "cooling break" in the curvature spectrum (the position of the break in the curvature spectrum does not depend on pulsar parameters, see Rudak & Dyks (1999) for details). To explain the lightcurves observed by EGRET, however, the polar cap model has to employ the problematic nearly aligned geometry or it has to abandon the spatial boundaries of the traditional polar gap, eg. by considering the slot gap model where acceleration continues to high altitude along the last open field lines (Arons 1983; Muslimov & Harding 2003a). Geometrically, however, this makes the polar cap model similar to the two-pole caustic model.

We conclude that the standard, low-altitude version of the polar cap model is not able to naturally explain the observed geometric properties of known gamma-ray pulsars. Given the firm position of the polar gap among the possible acceleration sites in the pulsar magnetosphere, however, it is still likely that the polar cap activity does take place, and that the narrow gamma-ray beam of the polar cap model will eventually be detected by GLAST.

3.4. Relative positions of radio and gamma-ray peaks

RY95 showed that the outer gap model is very successful in reproducing relative positions of radio and gamma-ray peaks in pulsar lightcurves (RY95). The two-pole caustic model works equally well for pulsars with wide peak separations (like Crab, Vela, and B1951+32). Moreover, the models naturally explain why such a large fraction of known gamma ray pulsars (~ 50 %) exhibit double peak lightcurves with a very wide separation between the peaks $\Delta^{\mathrm{peak}} \sim 0.4 - 0.5$.

Both these models imply that a single radio peak, which often slightly precedes in phase the first gamma-ray peak, is either a low altitude core component or (more probably) a cone component arising when our line of sight cuts through the edge of a cone of radio emission (hereafter we assume the terminology used for the "multiconal" model of radio emission pattern (Rankin 1993; Gil & Krawczyk 1996; Gangadhara & Gupta 2001; Kijak & Gil 2002), although a radio beam of *any* shape (eg. the "patchy" beam, Lyne & Manchester 1988) can be accommodated by the two-pole caustic and the OG model). The radio pulses of many young pulsars are now thought to be edges of cones or partial cones (Crawford et al. 2001; Crawford & Keim 2003).

The interpretation of the radio peaks as cones is much more probable than the core interpretation for two reasons: 1) all models of particular cases (Vela, Crab) employ relatively large impact angles $\beta = \zeta_{\mathrm{obs}} - \alpha$ (the minimal angles between the line of sight and the dipole axis); (eg. RY95 assume $\beta = -18°$ for the Crab (fig. 5 in RY95) and $\beta \approx 13°$ for the Vela (fig. 2 in RY95); CRZ2000 assume $\beta \approx 17°$ (fig. 7 in CRZ2000); we assume $\beta \approx 20°$ in Fig. 7 and $\beta \approx 6°$ in Fig. 9, this paper.) 2) in the case of the Crab pulsar the maximum slope of the position angle curve fitted to the radio data occurs just ahead of the low frequency component (hereafter LFC, Moffett & Hankins 1999), which precedes in phase the precursor component. The LFC appears to be closer to the dipole axis than the precursor (Fig. 12), which indicates that the latter is a cone (below we argue that it must be an *inner* cone). Unfortunately, this result is uncertain due to the poor quality of the fit within the main peak.

The Crab pulsar is an especially interesting case, because two of its radio peaks (the main peak MP, and the interpulse IP, Fig. 12) nearly coincide in phase with gamma-ray peaks P1 and P2. Assuming that this coincidence implies the same emission regions for radio and gamma-rays, it becomes possible to determine the location of the radio-emitting regions within the models of high-energy emission. Absolute timing analysis of the Crab pulsar performed recently in X-rays (Rots et al. 2000; Tennant et al. 2001; Kuiper et al. 2003) as well as in gamma-rays (Kuiper et al. 2001) revealed that the main radio peak of the Crab slightly lags in phase (by about 300 μs, ie. about 1% of the total phase) the maximum of the leading high-energy peak. This complicates the analysis because in general this lag can be interpreted in terms of either a different set of radio-emitting magnetic field lines (different r_{ovc}) or of different altitudes for the radio emission. To avoid these complications, we will first neglect the lag and assume that the main radio peaks of Crab (MP and IP) coincide with the two high-energy peaks. Possible interpretations of the lag will be given later in this section.

The radiation observed in the radio peaks that are (nearly) coincident in phase with the high-energy peaks should originate from the last open magnetic field lines (two-pole caustic model) or from lines lying very close to the last open field lines (with $r_{ovc} = 0.8 - 1.0$, outer gap model). Thus, the MP and the IP present the outermost cone, connected to the polar cap rim. We emphasize, that both the two-pole caustic and the outer gap model can accommodate the coincidence of radio and gamma peaks in two situations: 1) when the roughly uniform radio emission (per unit length of a magnetic field line) occurs within the entire acceleration region of a given model, and 2) when the radio emission regions are constrained only to those regions of the accelerator where the caustic peaks are formed. In the first case, the radio-emission would extend along the entire length of all last open magnetic field lines (two-pole caustic model) or along "nearly last" open field lines at all altitudes above the null charge surface (outer gap model). However, this possibility would require coherent processes at extremely different altitudes, and the radio emission would appear within the bridge and the offpulse region (the latter in the two-pole caustic model only), which is not observed in the radio lightcurves. In the second case, different radio frequencies can still be radiated at different altitudes within the caustic region, however, the radius-to-frequency mapping would not be apparent.

For the trailing peak (P2, or for IP in radio) the caustic regions are roughly the same in both models (two-pole caustic and OG), since the same caustic is responsible for producing P2 in the models. We find that in the case of the viewing geometry suited to reproduce the Crab's lightcurve, the trailing peak (and so the radio IP of the Crab) is produced at radial distances in the range $0.4 - 0.8R_{lc}$ (two-pole caustic model) and $0.2 - 0.6R_{lc}$ (OG model). Typical emission altitudes for the models are presented in Figs. 13 (two-pole caustic) and 14

(OG).

The origin of the main radio peak in the two models is completely different, as is the emission region for the leading gamma-ray peak. In the two-pole caustic model the P1 (or MP in radio) has exactly the same origin as P2 (or IP). Therefore, emission altitudes for P1 are only slightly lower than for P2 and typically fall in the range $0.3-0.6R_{lc}$ (Fig. 13). This slight difference results from a closer approach to a magnetic pole at P1 than at P2 (cf. Fig. 4). In the outer gap model, the main radio peak (and P1 in gamma-rays) is due to emission from the very vicinity of the light cylinder (at $\rho \sim R_{lc}$, Fig. 14, and often even at $r > R_{lc}$). This is in clear disagreement with estimates of radio emission altitudes (eg. Blaskiewicz et al. 1991; Kijak 2001; Gupta & Gangadhara 2003), although it must be remembered that the Crab does not fit in the radius-to-frequency mapping scheme. The radio precursor in the OG model comes from the opposite pole (and from much lower altitudes) than the main radio peak.

The radio emission only from the caustic regions is more acceptable in the case of the two-pole caustic model. The model is able to produce the gamma-ray-coincident radio peaks for a radio emission region which spans a *single* range of altitudes between $0.3-0.6R_{lc}$. If the radio emissivity in this region had been uniform in ϕ_m, a low-intensity bridge radio emission would be produced in this model (this may be easily inferred from Fig. 13 by determining the range of phases with emission altitudes in the range $0.3 - 0.6R_{lc}$). To avoid the bridge in radio, one would have to constrain the radio emission to the trailing part of the open field line cones (ie. to the regions which produce the two gamma-ray peaks in the two-pole caustic model). This is not unnatural, because radio lightcurves of many pulsars suggest azimuthal asymmetries in radio emission cones. These often include the lack of a leading part of the emission cone: Lyne & Manchester (1988) find that 30 % of asymmetric radio profiles consists of the trailing part of emission cones only.

In the case of the outer gap model, to avoid assuming radio emission from all altitudes above the null charge surface, *two* regions of radio emission are required: 1) between 0.8 and $1.0R_{lc}$ (for P1 and MP), and 2) somewhere between 0.2 and $0.6R_{lc}$ (for IP and P2). Had the radio emission from both these regions been uniform in ϕ_m, both of them would produce radio features within the bridge region (Fig. 14). To avoid this, one would have to assume that on the leading side of the open field line cone the radio emission only occurs close to the light cylinder (region 1), whereas on the trailing part only at low altitudes (region 2).

Thus, to explain the radio MP and IP peaks of the Crab within the two-pole caustic model, it is sufficient to assume that the intensity of radio emission is nonuniform in magnetic azimuth ϕ_m, which is not a stringent requirement. In the case of the outer gap model, it is necessary to assume that both radio emission altitudes, as well as the intensity of radio

emission are nonuniform in ϕ_{m}. Moreover, in the OG model, the main radio peak would have to be produced close to R_{lc} contrary to the precursor, which is assumed to originate from low altitudes and from the opposite magnetic pole than the main peak. We conclude that the gamma-ray-coincident radio peaks of the Crab pulsar speak in favour of the two-pole caustic model. They can be understood as emission from the last open magnetic field lines on the trailing part of the "polar cone", within the range of altitudes between ~ 0.3 and $\sim 0.6 R_{\mathrm{lc}}$. The Crab's precursor and the LFC are interpreted in this picture as inner conal components, with the LFC probably being the closest to the magnetic dipole axis.

To interpret the lag of the MP with respect to the high-energy leading peak (Kuiper et al. 2003 and references therein) it is necessary to determine r_{ovc} for the radio-emitting magnetic field lines, which would require detailed calculations of pair-formation fronts in the considered models. Making the simplest assumption, however, that the same set of field lines is responsible for both the high-energy and the radio emission, one can interpret the lag with the help of Figs. 13c (two-pole caustic model) and 14c (outer gap model). As can be inferred from Fig. 13c, in the case of the two-pole caustic model the maximum of the high-energy leading peak corresponds to $r \approx 0.5 R_{\mathrm{lc}}$ and the detection phase *increases* with increasing altitude (for the viewing geometry used in Fig. 13; for $\alpha = \zeta_{\mathrm{obs}} = 90°$ the detection phase at the trailing peak may *decrease* with altitude, depending on the considered altitude range, see. fig. 2 in Morini 1983). Therefore, the maximum of radio emission should occur at a slightly *larger* radial distance than the one corresponding to the *apparent* maximum of high-energy emission at the leading peak. Unlike in the case of the two-pole caustic model, according to the OG model, near the leading peak the phase of detection *decreases* with emission altitude (Fig. 14c, lower curve; the upper curve in Fig. 14c should not be considered since it corresponds to the emission from the very vicinity of the light cylinder). As noted by Kuiper et al. 2003, this implies that the maximum of radio emission must take place at a slightly *smaller* radial distance than the one which corresponds to the maximum of the observed high-energy leading peak ($r \approx 0.9 R_{\mathrm{lc}}$).

We emphasize that what we have just determined from the radio-to-high-energy lag is the *absolute* location of the radio emission region (which is $r \approx 0.5 R_{\mathrm{lc}}$ at the trailing side of the open field line region for the two-pole caustic model, and $r \approx 0.9 R_{\mathrm{lc}}$ at the leading side of the open volume for the OG model) — not the relative locations of the strongest high-energy and the radio emission regions. One should not, therefore, conclude that in the OG model the strongest X-ray emission takes place at larger altitudes than the strongest radio emission because in both models (two-pole caustic and OG) the high-energy emission is assumed to be uniform per unit length of a magnetic field line within a large range of altitudes, and the observed high-energy peaks are of purely caustic origin. In the case of both models, the spatially constrained region of the strongest radio emission is contained

entirely within the extended region of uniform high-energy emission.

Pulsars with two widely separated gamma-ray-peaks but without gamma-ray coincident radio peaks (like the Vela or B1951+32) apparently do not have the outermost radio cone related to the last open lines. The single radio peak preceding the leading gamma-ray peak arises from sampling radio emission from inner cones or core. Indeed, Gupta & Gangadhara (2003) find that in all pulsars they have studied the conal radio emission originates in the inner region of the open field line cone (with $r_{\rm ovc}$ between ~ 0.2 and ~ 0.8). The question of why some pulsars do not exhibit radio peaks coincident with high-energy peaks is apparently connected to the question of why some pulsars do not exhibit giant radio pulses. For three objects (the Crab, B1821$-$24, and B1937+21), all of which have radio peaks coincident with high-energy pulses, the giant radio pulses have been shown to coincide with the high-energy emission which suggests the same spatial origin in the magnetosphere (Romani & Johnston 2001; Cordes et al. 2003; Cusumano et al. 2003).

The polar cap model predicts that the two widely separated peaks of some gamma-ray pulsars arise when the line of sight crosses the narrow hollow cone of low altitude gamma ray emission. The nearly aligned geometry enables one to obtain large peak separation ($\Delta^{\rm peak} \sim 0.4 - 0.5$) in spite of the narrowness of the gamma-ray beam, ie. when $\alpha \sim \theta_\gamma$. Conal radio emission originates from higher altitudes than the hard gamma-rays, so the nested radio cones should surround the innermost gamma-ray cone. Therefore, there should be radio peaks preceding the leading gamma-ray peak, and following the trailing gamma-ray peak. Actually, only one radio peak is usually observed before the leading gamma-ray peak with no radio peak behind the trailing gamma-ray peak (the Vela, B1951+52). This can be explained by a commonly observed lack of trailing parts of radio cones: Lyne & Manchester (1988) find that 70 % of partial conal radio pulsars exhibit the lack of the trailing part of radio cones. However, nearly aligned radio pulsars normally exhibit very broad radio pulses (Lyne & Manchester 1988) which is not the case for the Vela and B1951+52. In fact, the width of the radio profile of the Vela pulsar is in perfect agreement with a low altitude emission from a rotator with a large dipole inclination (Rankin 1990). The large α was also determined for the Vela pulsar via analysis of the Chandra image of its X-ray nebula (Radhakrishnan & Deshpande 2001). The interpretation of the radio peak positions within the polar cap model is in conflict with these results.

4.   Conclusions

We find that none of the considered models can account for the observed variety of both pulsar lightcurves and polarization characteristics. The two-pole caustic model predicts

that the widely separated double peaks observed in the lightcurves of some pulsars are produced within altitude range between ~ 0.2 and $\sim 0.8R_{lc}$, where the dipolar structure of the magnetic field is well justified. The relative positions of radio and gamma-ray peaks in these lightcurves find a natural interpretation within the model. Interpretation of peaks in the radio pulse of the Crab pulsar is also possible within the two-pole caustic model. The detailed shape of the high-energy lightcurve of the Vela pulsar is a clear manifestation of the radiation pattern predicted generically by the two-pole caustic model although it must be understood why radio peaks coincident with high-energy peaks do not appear in Vela-like pulsars. However, the model is not able to reproduce double peak gamma-ray lightcurves with small peak separation (like those observed for B1706−44 and B1055−52, cf. Dyks & Rudak 2003) and the phase lag between the radio and the gamma-ray peak of B1509−58. It is also difficult to exactly reproduce ratios of peak intensity to the bridge, or offpulse intensity observed for the Crab and Vela pulsars by EGRET. The polarization characteristics predicted by the caustic model for some viewing parameters (fast swings of the position angle and minima in the polarization degree at both peaks) resemble those observed in the optical band for the Crab pulsar. Although exact agreement cannot be achieved under the assumptions of this paper, the approximate anticorrelation between the received flux and the polarization degree, visible in Figs. 7 and 8 is worth of notice. In addition to the Crab pulsar, the same anticorrelation has been observed in the optical band for B0656+14 (Kern et al. 2003), though the separation of ~ 0.6 between the optical peaks of this object cannot be easily interpreted within the two-pole caustic model. In the two-pole caustic model, the minima of $P[\%]$ associated with the peaks result naturally from the superposition of radiation originating from different altitudes – the same superposition which produces the peaks themselves. This depolarization is efficient only when some spatial spread in electron density around the last open magnetic field lines is assumed. In addition to this "caustic depolarization", there are other minima in $P[\%]$ which appear close to the peaks – these are caused by the superposition of the two radiation patterns associated with the opposite magnetic poles.

The position angle curves predicted by the outer gap model do not resemble the PA curve observed for the Crab. The outer gap model naturally explains the lightcurves except for the off-pulse emission, however, it predicts that the leading gamma-ray peak is produced close to the light cylinder, and strongly relies on the geometry of magnetic field in this region. To explain the radio properties of the Crab pulsar, the outer gap model must locate the radio emission regions at a variety of positions in the magnetosphere.

The polar cap model requires improbably precise adjustment of viewing geometry to reproduce observed separations of double peaks in pulsar lightcurves. It does not predict fast position angle swings at the peaks.

Based on comparison of the predicted and the observed lightcurves, we find that the two-pole caustic model and the outer gap model are most successful, although only the two-pole caustic model is reliable from the point of view of the moderate emission altitudes involved. The results described above support the idea that the observed high-energy emission from at least some gamma-ray pulsars (eg. Vela, Crab) has its origin in the outer magnetosphere. However, the results suggest that the high-energy lightcurves of these pulsars find more natural explanation within the geometry of the two-pole caustic model rather than within the outer gap model. The physical basis of the two-pole caustic model may well find its origin in extended slot gap acceleration (Muslimov & Harding 2003b). The discrepancies between the polarization characteristics calculated in this paper and the Crab data do not necessarily disprove the considered models for three reasons: 1) Our polarization results are determined purely by the geometry of the magnetic field, and do not take into account the frequency dependence of polarization characteristics (eg. Epstein 1973; Chen et al. 1996). 2) the Crab pulsar is the *only* case for which the high-energy polarization data are available. 3) Polarization characteristics of the pulsed emission from the Crab pulsar may by affected by the choice of Stokes parameters for the constant component which is subtracted from the total signal.

The apparently constant position angle of the constant component of Crab optical emission (Kanbach et al. 2003) is an astonishing feature which may be interpreted in two ways: 1) it may be a contribution from a separate source, not related to the pulsar magnetosphere (unresolved wisp of the Crab nebula?, some background object?); 2) it may present emission from a beyond-$R_{\rm lc}$ region of the rotating/outflowing dipolar magnetosphere of the Crab pulsar. The second interpretation is possible because in the region beyond the light cylinder the magnetic field is dominated by a toroidal component, and the orientation of a toroidal vector with respect to the rotation axis is fixed regardless of the rotational phase (Smith et al. 1988). Indeed, Radhakrishnan & Deshpande (2001) proposed a model for a Chandra X-ray image of the Vela pulsar, which implies existence of an apparent, linearly polarized "jet" aligned with the pulsar rotation axis. The origin of the "jet" is the synchrotron radiation from a region beyond the light cylinder. The authors note that a similar, as yet spatially unresolved structure (at X-rays) may surround the Crab pulsar. Had the synchrotron emission of the "jet" extended down to the optical band, it could possibly account for the observed properties of the constant component of the Crab's optical emission. However, it would still have to stay spatially unresolved even in the optical band.

Assuming the second interpretation is correct, one could explain the total (pulsed + constant) optical emission from the Crab pulsar as a blend of the pulsed signal predicted by the two-pole caustic model and the constant emission from the beyond-$R_{\rm lc}$ region. We find that adding a constant component to the theoretical lightcurve of the two-pole caustic

model does produce the "zigzag" shape of position angle curve at the leading peak.

On the other hand, the two component model of optical emission from Crab (Kellner 2002) is a model only, and it is possible that the total emission is not a blend of two sources widely separated in space, but reflects the geometry of a single emission region located beyond the light cylinder. In the latter case extracting the pulsed component from the total data would be misleading. Possibly the wind model by Kirk et al. (2002) offers an example for a source of radiation which produces fixed position angle at all phases except from those at which the peaks occur. In the model, high-energy radiation is emitted at large distances from the star ($10-100R_{\rm lc}$) at current sheets, which separate "layers" of the toroidal magnetic field. The direction of the magnetic field is nearly the same at all points within a layer, and it changes by 180° at the current sheets. The sheets are the place where the magnetic energy is dissipated into particle energy (reconnection), and from which the radiation observed at peaks origins. The pulses are observed because the consecutive sheets move relativistically towards an observer. Had the electric field vector of radiation emitted at the sheets changed its direction by 180° (as the direction of $\vec{B}$ does) a fast swing of position angle would be observed at the peaks. Moreover, a disorder in $\vec{B}$ direction within the reconnection region could produce a significant depolarization at the peaks. Unfortunately, calculations of pulsar polarization properties have not been performed so far for the wind model.

Finally, let us recall two technical, but interesting results of this paper: 1) For the case of the magnetic field structure described by the rotating/retarded dipole, and for moderate inclination angles $\alpha \simeq 40° - 50°$, the polar cap possesses a "notch". At the notch, the magnetic colatitude of the polar cap rim is not a single-valued function of magnetic azimuth. 2) Rotational distortions of the magnetic field result in low-altitude deformations of polar cap radiation beam which have magnitude larger than the effects of aberration and propagation time delays ($\sim \beta_{\rm cor}$).

REFERENCES

Arendt, P. N., & Eilek, J. A. 1998, ApJ, submitted (astro-ph/9801257)

Arons, J. 1983, ApJ, 266, 215

Arons, J., & Scharlemann E. T. 1979, ApJ, 231, 854

Baring, M. G. 2001, in Astrophysics and Space Science Library 267, Proc. Tonantzintla Workshop, ed. A. Carramiñana et al. (Dordrecht), 167

Blaskiewicz, M., Cordes, J. M., & Wasserman, I. 1991, ApJ, 370, 643 (BCW91)

Bloser, P. F., Hunter, S. D., Depaola, G. O., & Longo, F. 2003, in Proc. SPIE 5165, "X-ray and Gamma-Ray Instrumentation for Astronomy XIII", in press

Chen, K., Chang, H.-K., & Ho, C. 1996, ApJ, 471, 967

Cheng, K. S., Ho, C., & Ruderman, M. 1986, ApJ, 300, 500

Cheng, K. S., Ruderman, M. A., & Zhang, L. 2000, ApJ, 537, 964 (CRZ2000)

Cordes, J. M., Bhat, N. D. R., Hankins, T. H., McLaughlin, M. A., & Kern, J. 2003, ApJ, submitted (astro-ph/0304495)

Crawford, F., & Keim, N. C. 2003, ApJ, 590, 1020

Crawford, F., Manchester, R. N., & Kaspi, V. M. 1991, AJ, 122, 2001

Cusumano, G., Hermsen, W., Kramer, M., Kuiper, L., Löhmer, O., et al. 2003, A&A, submitted (astro-ph/0309580)

Damour, T., & Taylor, J. H. 1992, Phys. Rev. D, 45, 1840

Daugherty, J.K., & Harding, A.K. 1982, ApJ, 252, 337

Daugherty, J.K., & Harding, A.K. 1994, ApJ, 42, 325

Daugherty, J.K., & Harding, A.K. 1996, ApJ, 458, 278

Dyks, J. 2002, PhD Thesis, Nicolaus Copernicus Astronomical Center

Dyks, J., & Rudak, B. 2000, MNRAS, 319, 477

Dyks, J., & Rudak, B. 2002, A&A, 393, 511

Dyks, J., & Rudak, B. 2003, ApJ, 598, 1201

Epstein, R. I. 1973, ApJ, 183, 593

Everett, J. E., & Weisberg, J. M. 2001, ApJ, 553, 341 (EW2001)

Fierro, J. M. 1996, PhD Thesis, Stanford University

Gangadhara, R. T., & Gupta, Y. 2001, ApJ, 555, 31

Gil, J., Khechinashvili, D. G., & Melikidze, G. I. 1998, MNRAS, 298, 1207

Gil, J., & Krawczyk, A. 1996, MNRAS, 280, 143

Graham-Smith, F., Dolan, J. F., Boyd, P. T., Biggs, J. D., Lyne, A. G., et al. 1996, MNRAS, 282, 1354

Grenier, I. A., Hermsen, A., & Clear, J. 1988, A&A, 204, 117

Gupta, Y., & Gangadhara, R. T. 2003, ApJ, 584, 418

Harding, A. K., Tademaru, E., & Esposito, L. W. 1978, ApJ, 225, 226

Helfand, D. J., Gotthelf, E. V., & Halpern, J. P. 2001, ApJ, 556, 380

Hester, J. J., Scowen, P. A., Sankrit, R., Burrows, C. J., Gallagher III, J. S., et al. 1995, ApJ, 448, 240

Hibschman, J. A., & Arons, J. 2001, ApJ, 546, 382 (HA2001)

Hirotani, K., & Shibata, S., 2001, MNRAS, 325, 1228

Hirotani, K., Harding, A.K., & Shibata, S. 2003, ApJ, 591, 334

Johnston, S., van Straten, W., Kramer, M., & Bailes, M. 2001, ApJ, 549, L101

Jones, D. H. P., Smith, F. G., & Wallace, P. T. 1981, MNRAS, 196, 943

Kanbach, G., Arzoumanian, Z., Bertsch, D. L., Brazier, K. T. S., Chiang, J., et al. 1994, A&A, 289, 855

Kanbach, G. 1999, in Astroph. Lett. Comm. 38, Proc. of the Third INTEGRAL Workshop, 17

Kanbach, G., Kellner, S., Schrey, F., Steinle, H., Straubmeier, C., et al. 2003, SPIE Meeting on Astronomical Telescopes and Instrumentation "Power Telescopes and Instrumentation into the New Millenium", eds. Iye, M., & Moorwood, A. F., 4841, 82

Kellner, S. 2002, Diplomarbeit, Technische Universität München (http://www.mpe.mpg.de/gamma/instruments/optima/www/optima-papers.html)

Kern, B., Martin, C., Mazin, B., & Halpern, J. P. 2003, ApJ, accepted (ApJ preprint doi:10.1086/378670)

Kijak, J. 2001, MNRAS, 323, 537

Kijak, J., & Gil, J. 2002, A&A, 392, 189

Kirk, J. G., Skjaeraasen, O., & Gallant, Y. A. 2002, A&A, 388, L29

Krishnamohan, S., & Downs, G. S. 1983, ApJ, 265, 372

Kuiper, L., Hermsen, W., Cusumano, G., Diehl, R., Schönfelder, V., et al. 2001, A&A, 378, 918

Kuiper, L., Hermsen, W., Walter, R., & Foschini, L. 2003, A&A, submitted (astro-ph/0309178)

Lai, D., Chernoff, D. F., & Cordes, J. M. 2001, ApJ, 549, 1111

Lyne, A. G., & Manchester, R. N. 1988, MNRAS, 234, 477

Malofeev, V. M. 1998, Astron. Zh., 75, 281

Malofeev, V. M., & Malov, O. I. 2000, Astron. Zh., 77, 52

Massaro, E., Salvati, M., & Buccheri, R. 1979, MNRAS, 189, 823

Moffett, D. A., & Hankins, T. H. 1996, ApJ, 468, 779

Moffett, D. A., & Hankins, T. H. 1999, ApJ, 522, 1046

Morini, M. 1983, MNRAS, 202, 495

Muslimov, A. G., & Harding, A. K. 2003a, ApJ, 588, 430

Muslimov, A. G., & Harding, A. K. 2003b, ApJ, submitted

Pavlov, G. G., Sanval, D., Garmire, G. P., Zavlin, V. E., Burwitz, V., et al. 2000, AAS Meeting, 196, 37.04

Radhakrishnan, V., & Cooke, D. J. 1969, Astrophys. Lett., 3, 225

Radhakrishnan, V., & Deshpande, A. A. 2001, A&A, 379, 551

Rankin, J. M. 1990, ApJ, 352, 247

Rankin, J. M. 1993, ApJ, 405, 285

Romani, R. W., & Johnston, S. 2001, ApJ, 590, L95

Romani, R. W., Miller, A. J., Cabrera, B., Nam, S. W., & Martinis, J. M. 2001, ApJ, 563, 221

Romani, R. W. & Yadigaroglu, I.-A., 1995, ApJ, 438, 314 (RY95)

Rots, A. H., Jahoda, K., & Lyne, A. G. 2000, AAS HEAD Meeting, 32, 3308

Rudak, B., & Dyks, J. 1999, MNRAS, 303, 477

Ruderman, M. A., & Sutherland, P. G. 1975, ApJ, 196, 51

Smith, F. G., Jones, D. H. P., Dick, J. S. B., & Pike, C. D. 1988, MNRAS, 233, 305

Sturner, S. J., Dermer, C. D., & Michel, F. C. 1995, ApJ, 445, 736

Sturrock, P. A. 1971, ApJ, 164, 529

Tennant, A. F., Becker, W., Juda, M., Elsner, R. F., Kolodziejczak, J. J., et al. 2001, ApJ, 554, L173

Thompson, D. J. 2001, in AIP Proceedings 558, High Energy Gamma-Ray Astronomy, ed. A. Goldwurm et al., 103

Wright, G. A. E. 2003, MNRAS, 344, 1041

Yadigaroglu, I.-A. 1997, Ph.D. thesis, Stanford University

Table 1.   Symmetries of the position angle curve with respect to the transformations $\alpha \to \pi - \alpha$ and $\zeta_{\mathrm{obs}} \to \pi - \zeta_{\mathrm{obs}}$. The third column gives the PA curve $\psi'(\phi)$ which is recorded by an observer located at ζ'_{obs} and who is viewing a pulsar with the magnetic dipole tilted at the angle α' with respect to the positive rotational axis, *if* another observer (located at ζ_{obs} and viewing the dipole tilted at α) records the PA curve $\psi(\phi)$.

α'	ζ'_{obs}	$\psi'(\phi)$
α	$\pi - \zeta_{\mathrm{obs}}$	$-\psi(\phi + \pi)$
$\pi - \alpha$	ζ_{obs}	$\psi(\phi + \pi)$
$\pi - \alpha$	$\pi - \zeta_{\mathrm{obs}}$	$-\psi(\phi)$
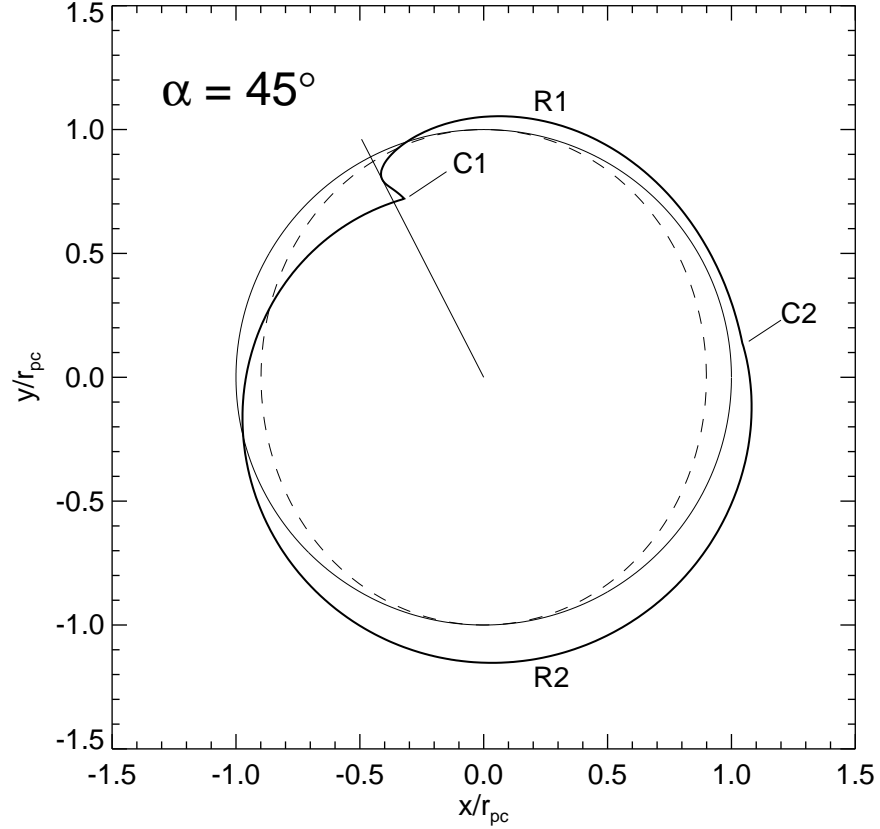
Fig. 1.— Two polar caps for a dipole tilted at $\alpha = 45°$ and rotation period $P_{\rm rot} = 0.033$ s: Thick solid line (with a notch) presents the polar cap rim for the retarded dipole. The dashed oval is for the static shape dipole. A circle of radius $r_{\rm pc}$ (corresponding to a polar cap of a dipole aligned with rotation axis) is added for a reference (thin solid). Note that for most azimuths, the circle approximates the retarded case (thick solid) better than the actual rim of the cap for static dipole (dashed). The magnetic azimuth $\phi_{\rm m}$ is measured counterclockwise from positive x axis. The closest rotational pole is on the left ($\phi_{\rm m} = 180°$). The corotational velocity points upwards ($\phi_{\rm m} = 90°$). In this figure, as well as in Figs. 2 and 3, the magnetic moment $\vec{\mu}$ of the retarded dipole is aligned with the magnetic moment of the static dipole ($\vec{\mu}$ is located perpendicularly to the page at the point $(x, y) = (0, 0)$).
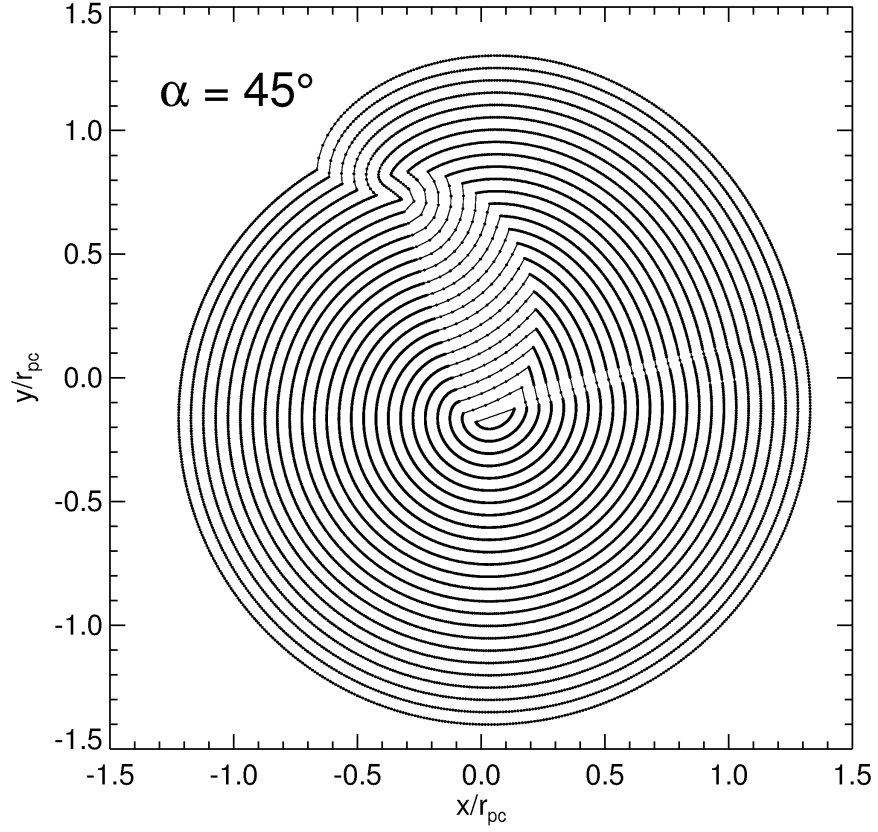
Fig. 2.— The grid of constant open volume coordinate r_{ovc} for $\alpha = 45°$ and $P_{rot} = 0.033$ s. The values of r_{ovc} range between 0.05 (innermost ring) and 1.25 (outermost) and the distance between them is 0.05. The sixth ring (counting inwards) is the rim of the polar cap (shown with a thick solid line in previous figure).
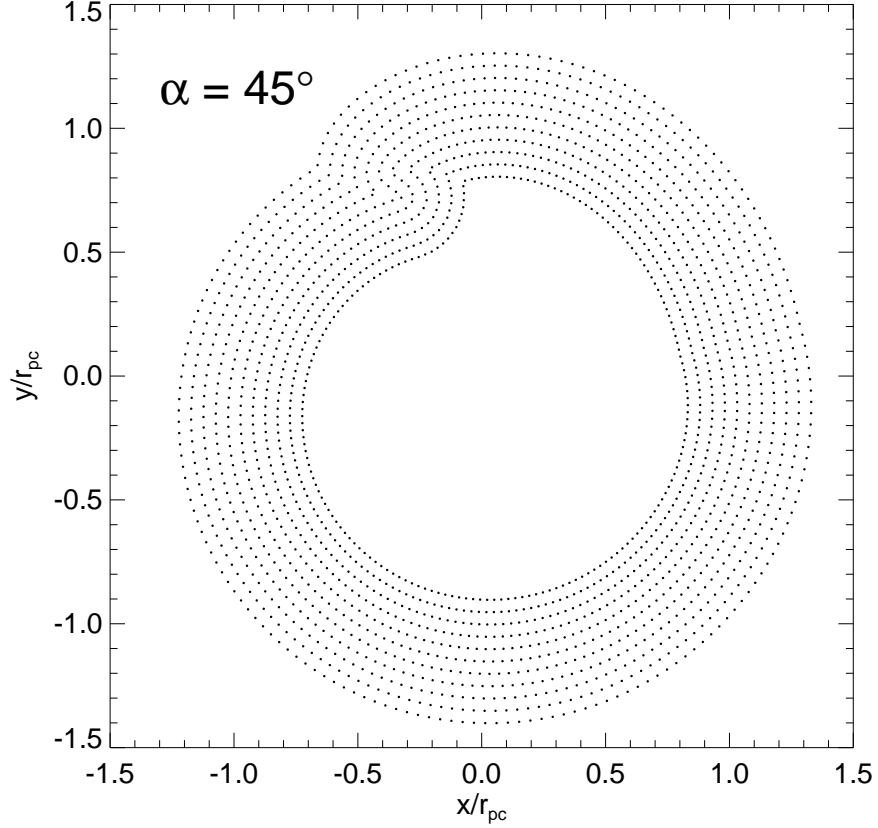
Fig. 3.— Sample distribution of footprints of magnetic field lines along which photon emission is modelled (for $\alpha = 45°$ and $P_{\rm rot} = 0.033$ s). There are 180 footprint points uniformly distributed along each ring of constant $r_{\rm ovc}$, with the latter in the range between 0.75 and 1.25. The rings are separated by 0.05. In calculations described in Section 3 we usually take a narrower range of $r_{\rm ovc}$ $(0.95 - 1.05)$ with smaller ring separation of 0.005, and with 1800 footprints per ring.
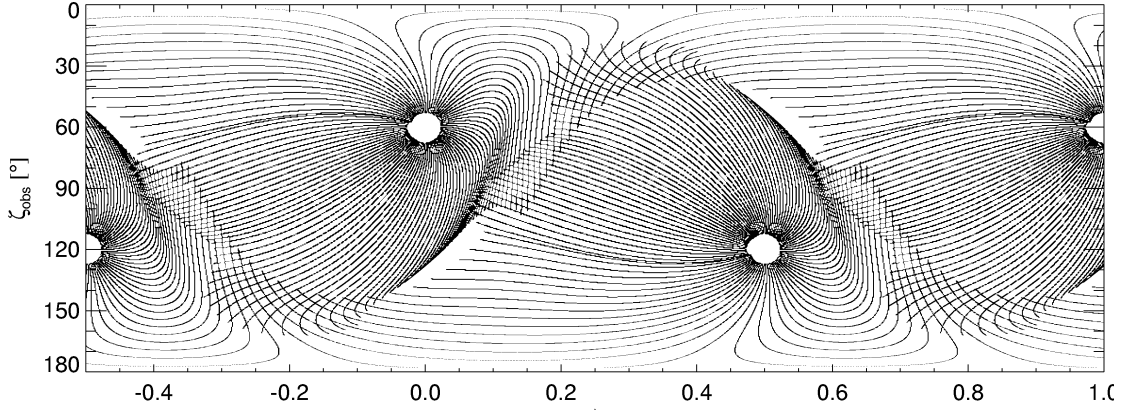
Fig. 4.— Projection of the last open magnetic field lines of rotating retarded dipole on the space $(\phi, \zeta_{\mathrm{obs}})$ for $\alpha = 60°$. Note two strong caustics (dark arches) trailing both polar caps (blank deformed ovals). They form because aberration and propagation time effects tend to pile up at nearly the same phase photons emitted from different altitudes. A horizontal cut of this pattern by an observer located at a fixed ζ_{obs} produces a lightcurve with two widely separated peaks. The pattern was calculated for $r_{\mathrm{ovc}} = 1$, $\rho_{\mathrm{max}} = 0.75 R_{\mathrm{lc}}$, $r_{\mathrm{max}} = R_{\mathrm{lc}}$, and $P_{\mathrm{rot}} = 0.033$ s. Only the size of polar caps depends on the rotation period P_{rot}.
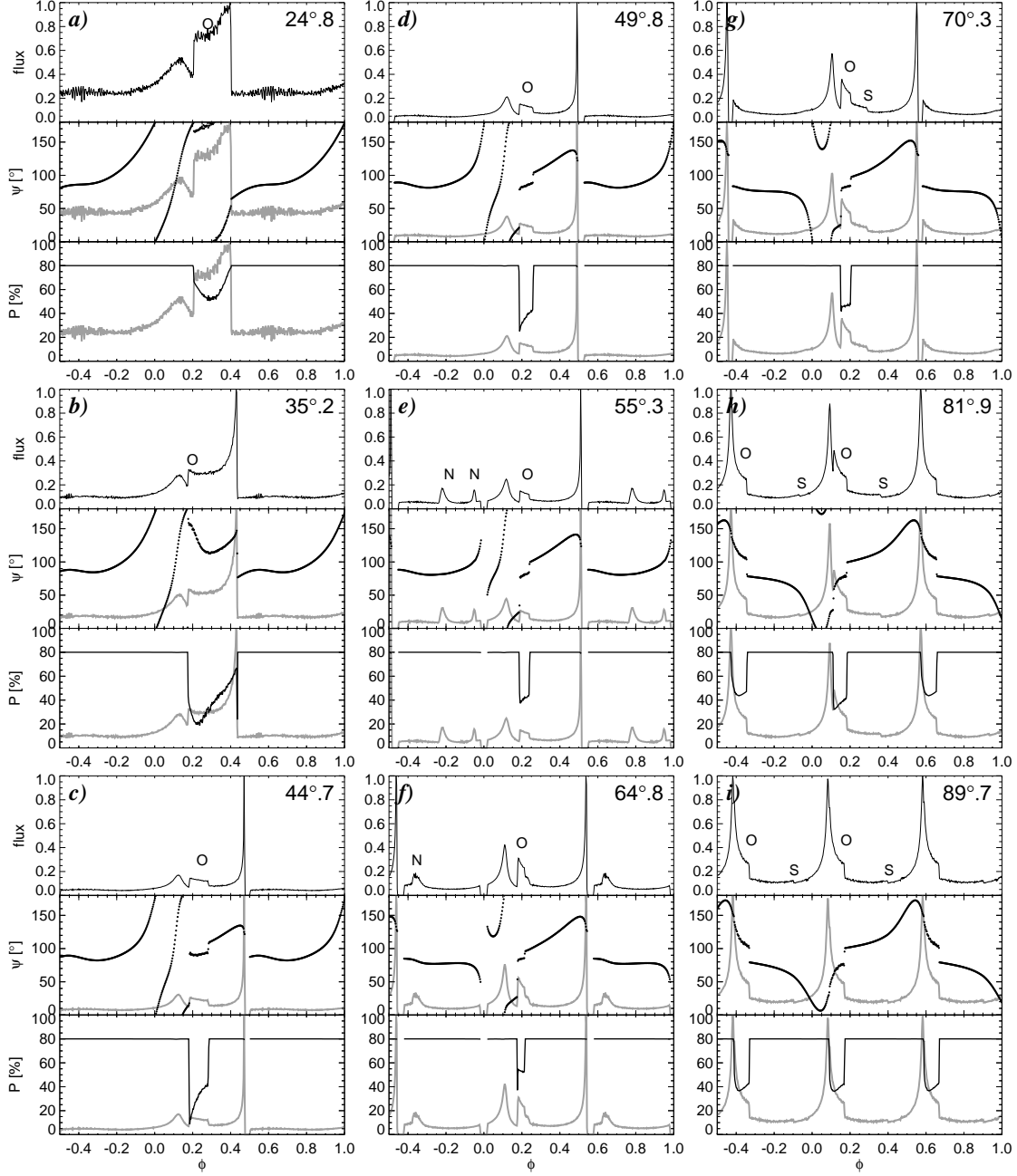
Fig. 5.— Radiation characteristics predicted by the two-pole caustic model for a pulsar with dipole inclination $\alpha = 60°$. Nine three-panel frames correspond to nine different viewing angles ζ_{obs} (marked in the top right corners). Each frame presents the lightcurve (top panel), the position angle curve (dots, middle panel), and the degree of linear polarization (thick solid line, bottom panel). For reference, the lightcurve is overplotted in the middle and in the bottom panels as a thick grey line. Features marked with N, O, and S are described in the text. Note the dominance of two widely separated peaks in lightcurves for most viewing angles, and a fast swing of position angle at the first peak for $\zeta_{obs} \lesssim 70°$. The results are for $\rho_{max} = 0.75 R_{lc}$, $r_{max} = R_{lc}$, $r_{ovc} = 1$, and $P_{rot} = 0.033$ s.
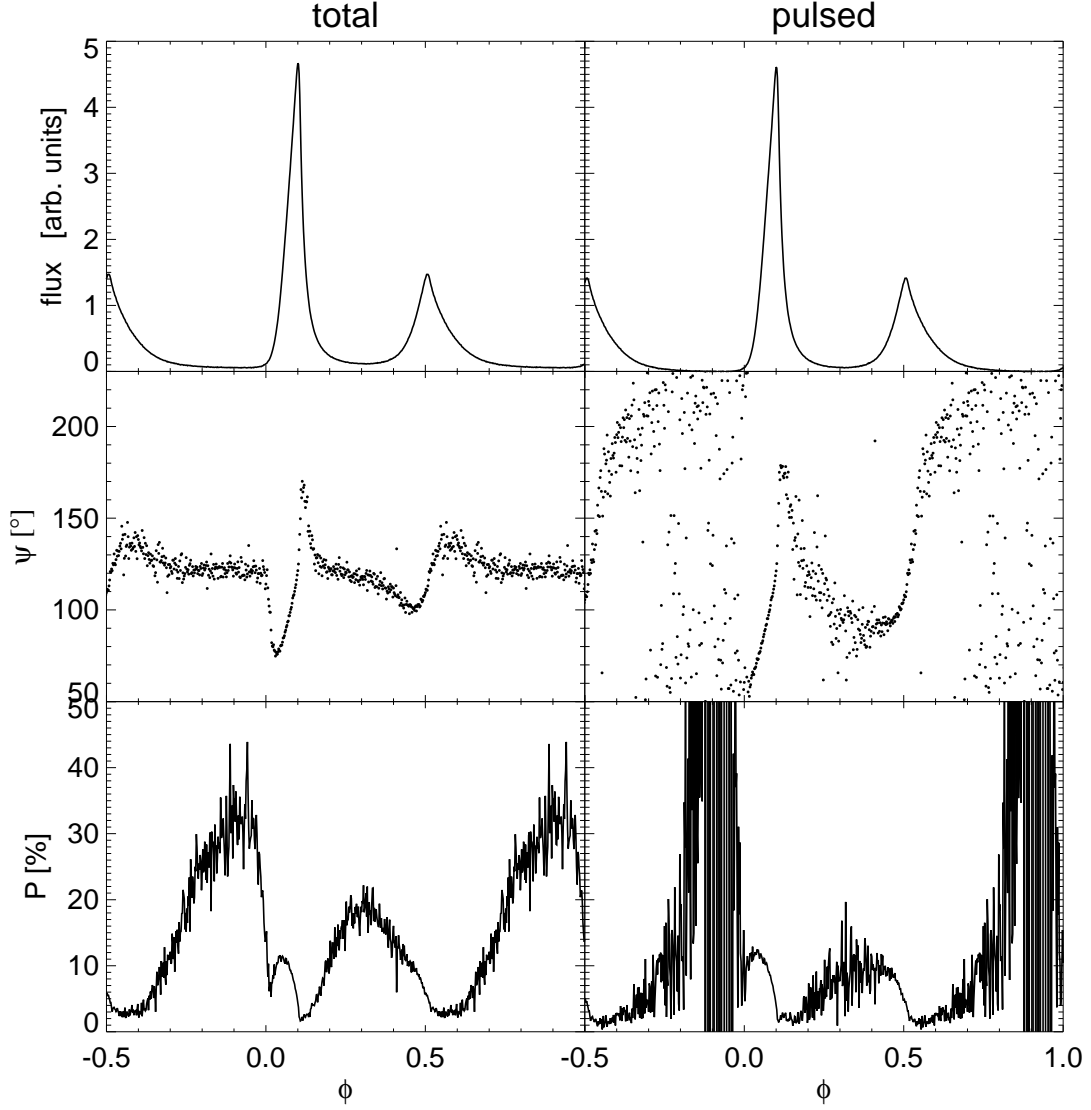
Fig. 6.— Preliminary optical data on the Crab pulsar obtained with the OPTIMA instrument (Kanbach et al. 2003). Left column: a lightcurve (top panel), a position angle ψ (dots, middle panel), and a degree of polarization P (bottom panel). The constant value of position angle within phase ranges $0.6 - 0.9$ and $1.1 - 1.2$ suggests that the received radiation consists of two components, one of which has constant properties. Right column: same as in the left column but with the contribution of the constant component subtracted from the data. Following Kellner (2002), for the constant component we assumed intensity equal to 1.24 % of the maximum intensity of the total signal, $\psi = 123°$, and $P = 33$ %. One and a half period is shown. The maximum of the leading peak was aligned with the phase $\phi = 0.1$. The data were kindly provided by G. Kanbach.
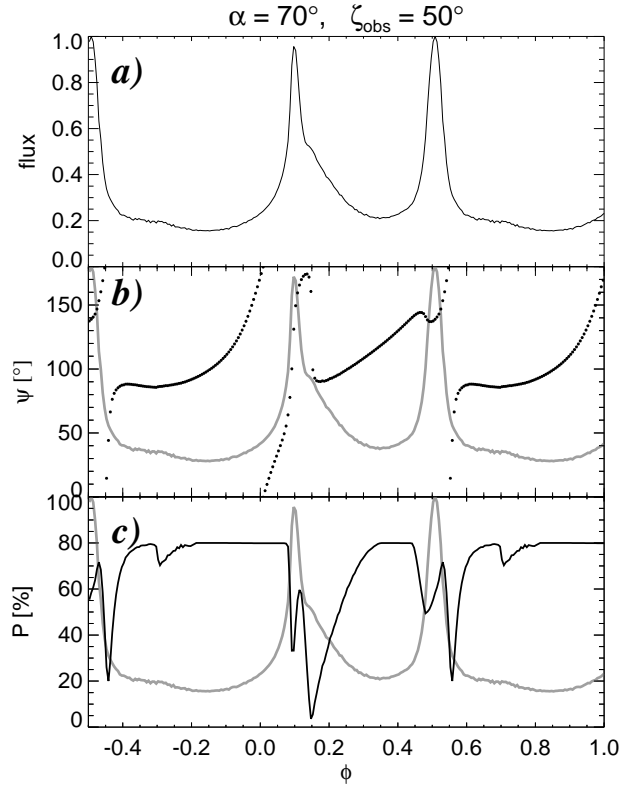
Fig. 7.— A lightcurve (a), a position angle (points, b), and a degree of polarization (thick solid line, c) predicted by the two-pole caustic model for $\alpha = 70°$ and $\zeta_{obs} = 50°$. A spread in electron density at the star surface was assumed ($\sigma = 0.025$, $r_{ovc}^{0} = 1$, $r_{ovc}^{min} = 0.95$, $r_{ovc}^{max} = 1.05$) and $\rho_{max} = 0.8R_{lc}$, $r_{max} = R_{lc}$. The results are for the retarded dipole field.
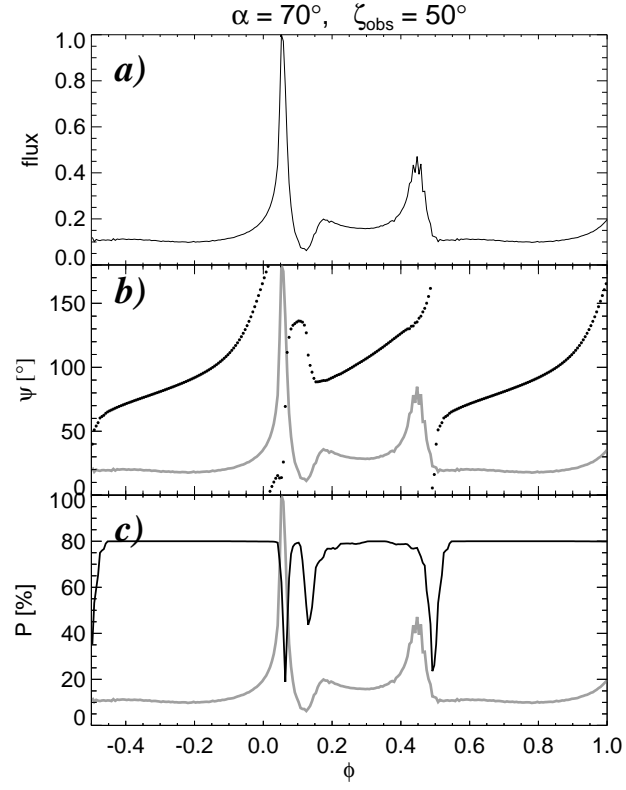
Fig. 8.— Two-pole caustic model results obtained for the same parameters as in Fig. 7, but for the static shape dipole with the circular polar cap rim. Note the similarity of both these cases.
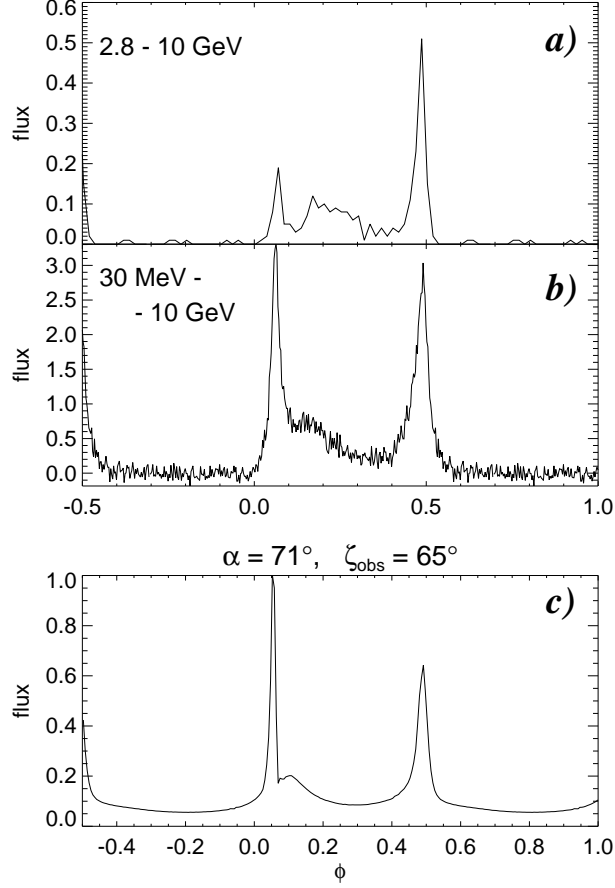
Fig. 9.— Two upper panels present gamma ray lightcurves observed for the Vela pulsar by EGRET (Kanbach 1999) in two different photon energy ranges: between 2.8 and 10 GeV (a) and between 30 MeV and 10 GeV (b). Panel c presents a lightcurve predicted by the two-pole caustic model for $\alpha = 71°$, $\zeta_{obs} = 65°$, $r_{max} = \rho_{max} = 0.95 R_{lc}$, and $P_{rot} = 0.0893$ s. The lightcurve was calculated for the static shape dipole with the circular polar cap and for a spread in the electron density at the star surface with $\sigma = 0.025$, $r_{ovc}^0 = 1$, $r_{ovc}^{min} = 0.95$ and $r_{ovc}^{max} = 1.05$. Note the similarity of the model lightcurve (c) to the one observed within the entire energy band of EGRET (b).
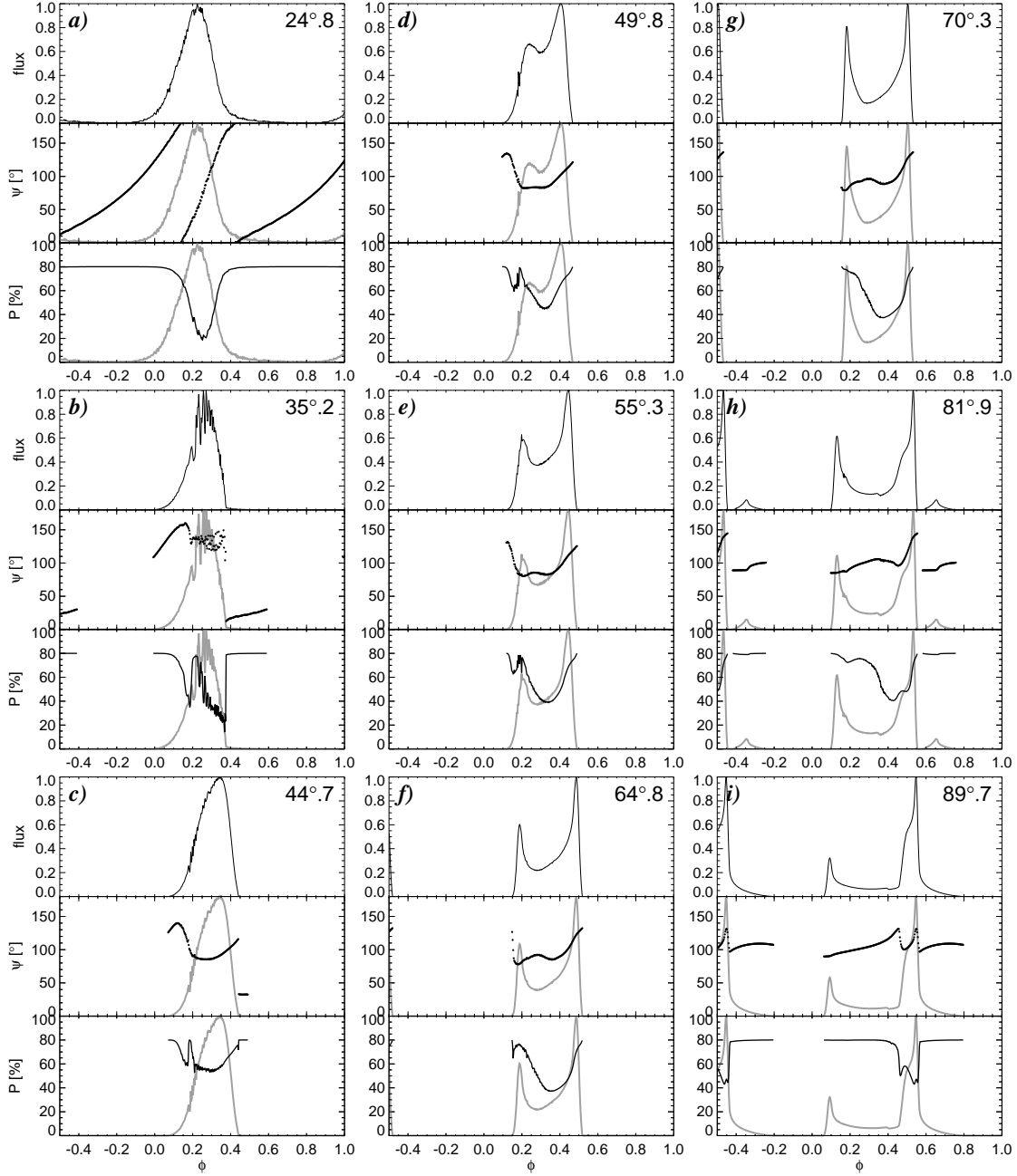
Fig. 10.— Radiation characteristics predicted by the outer gap model for a pulsar with magnetic dipole inclination $\alpha = 65°$. The layout is the same as in Fig. 5. The results have been obtained for $r_{\mathrm{ovc}} = 0.9$, $\rho_{\max} = 0.999 R_{\mathrm{lc}}$, $r_{\max} = 1.7 R_{\mathrm{lc}}$, $P_{\mathrm{rot}} = 0.033$ s, and the electron density spread with $\sigma = 0.025$, $r_{\mathrm{ovc}}^0 = 0.9$, $r_{\mathrm{ovc}}^{\min} = 0.85$, and $r_{\mathrm{ovc}}^{\max} = 0.95$.

polar cap, α=7°, ζ=12°
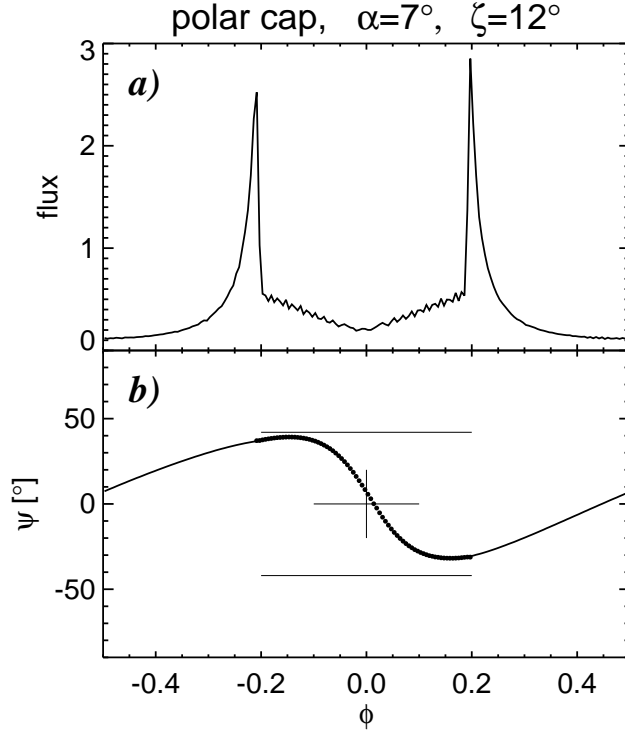
Fig. 11.— Panel a: a gamma-ray lightcurve predicted by the polar cap model for $\alpha = 7°$, $\zeta_{\rm obs} = 12°$, $P_{\rm rot} = 0.033$ s, and an accelerator at radial distance $r = 3R_{\rm ns}$. Panel b: position angle curve. The central, dotted part of the PA curve ($|\phi| \lesssim 0.2$) was calculated for photon emission from the fixed radial distance $r = 3R_{\rm ns}$. The rest is for emission from the last open field lines at $r \geq 3R_{\rm ns}$. The cross centered at $(\phi, \psi) = (0, 0)$ and the two horizontals at $\psi = \pm 42°$ provide reference to discern the influence of rotation on the PA curve (see the text for details). The results are for the static shape dipole with the circular polar cap.
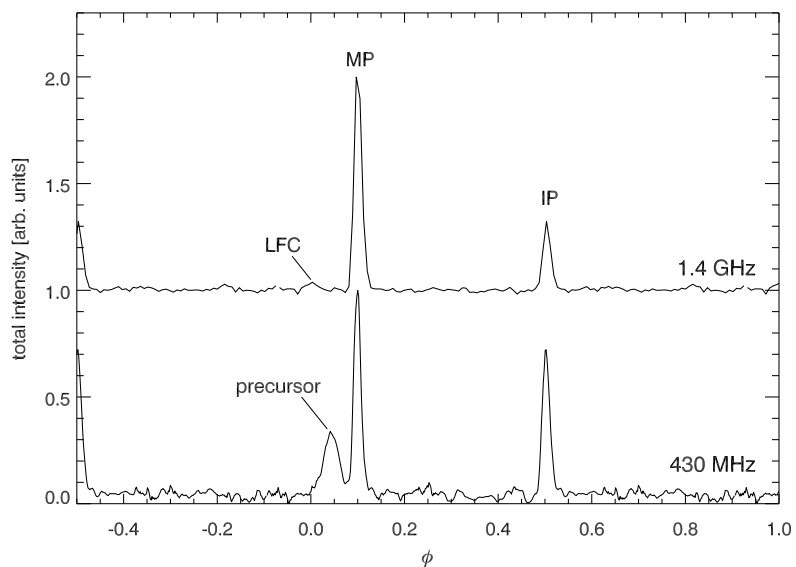
Fig. 12.— Radio pulse profiles of the Crab pulsar at 1.4 GHz (upper curve) and 430 MHz (lower curve). The pulse features discussed in Section 3.4 are identified. One and a half period is shown. The main peak (MP) of the profiles was aligned with the phase $\phi = 0.1$. The data are from Moffett & Hankins (1996).
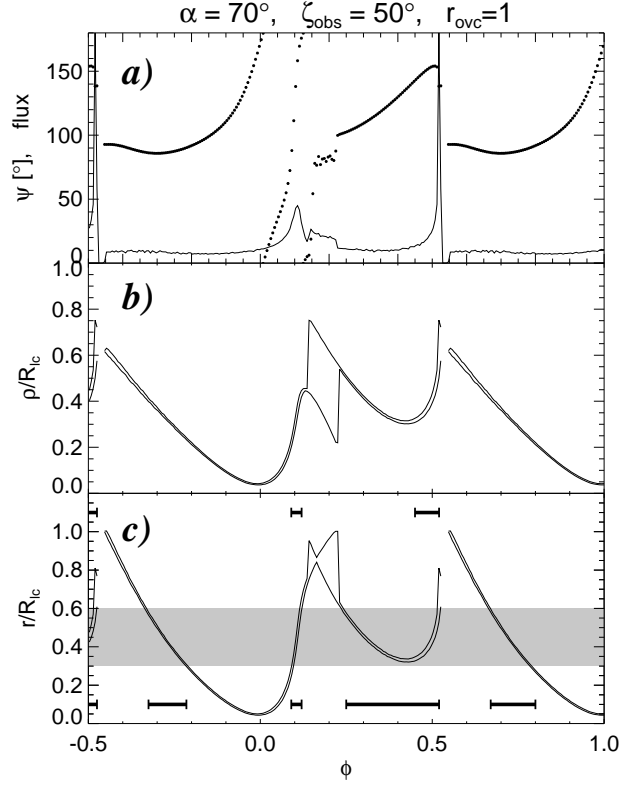
Fig. 13.— Panel a: a lightcurve (solid line), and a position angle curve (dots) predicted by the two-pole caustic model for $\alpha = 70°$, $\zeta_{obs} = 50°$, $r_{ovc} = 1$, $\rho_{max} = 0.75R_{lc}$ and $r_{max} = R_{lc}$. Panel b: the distance ρ of emission points from the rotation axis as a function of phase ϕ at which the radiation emitted at these points is detected. The bottom curve is for the minimum value of the distance, the top curve is for the maximum distance. Panel c: the radial distance r of emission points from the star center as a function of the detection phase ϕ. The bottom curve is for the minimum value of r, the top line – for the maximum r. The shaded band denotes the range of r from which coherent radio waves should be emitted in order for radio peaks to coincide with the gamma-ray peaks visible in panel a. Projection of those fragments of the $r(\phi)$ curves which cross the shaded band onto the horizontal axis determines ranges of phase within which radio emission would be observed (marked with horizontal bars near the bottom horizontal axis). In addition to the radio peaks at $\phi = 0.1$ and $\phi = 0.5$, a bridge, and an offpulse radio emission would be observed. If only a trailing part of radio emission cones existed, the radio emission from the outermost cones would be observed only at phases coincident with the gamma ray peaks (horizontal bars near the top horizontal axis). Radio emission from inner cones could produce the LFC and the radio precursor.
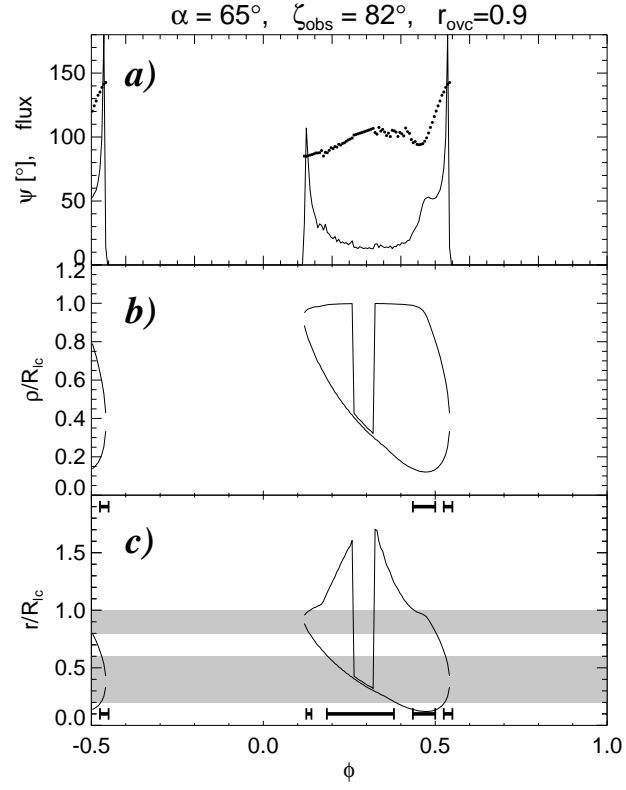
Fig. 14.— The same as in Fig. 13 but for the outer gap model with $\alpha = 65°$, $\zeta_{obs} = 82°$, $r_{ovc} = 0.9$, $\rho_{max} = 0.999 R_{lc}$, and $r_{max} = 1.7 R_{lc}$ (the same parameters as in Fig. 7 of CRZ2000).